PHYSICAL REVIEW A **106**, 022615 (2022)

Numerical analysis of effective models for flux-tunable transmon systems

H. Lagemann,[1,2,*] D. Willsch,[1] M. Willsch,[1] F. Jin,[1] H. De Raedt,[1,3] and K. Michielsen[1,2]
[1]*Institute for Advanced Simulation, Jülich Supercomputing Centre, Forschungszentrum Jülich, D-52425 Jülich, Germany*
[2]*RWTH Aachen University, D-52056 Aachen, Germany*
[3]*Zernike Institute for Advanced Materials, University of Groningen, Nijenborgh 4, NL-9747 AG Groningen, The Netherlands*

(Received 11 January 2022; revised 12 May 2022; accepted 7 July 2022; published 26 August 2022)

Simulations and analytical calculations that aim to describe flux-tunable transmons are usually based on effective models of the corresponding lumped-element model. However, when a control pulse is applied, in most cases it is not known how much the predictions made with the effective models deviate from the predictions made with the original lumped-element model. In this work we compare the numerical solutions of the time-dependent Schrödinger equation for both the effective and the lumped-element models, for microwave and unimodal control pulses (external fluxes). These control pulses are used to model single-qubit (X) and two-qubit gate (iSWAP and CZ) transitions. First, we derive a nonadiabatic effective Hamiltonian for a single flux-tunable transmon and compare the pulse response of this model to the one of the corresponding circuit Hamiltonian. Here we find that both models predict similar outcomes for similar control pulses. Then, we study how different approximations affect single-qubit (X) and two-qubit gate (iSWAP and CZ) transitions in two different two-qubit systems. For this purpose we consider three different systems in total: a single flux-tunable transmon and two two-qubit systems. In summary, we find that a series of commonly applied approximations (individually and/or in combination) can change the response of a system substantially, when a control pulse is applied.

DOI: 10.1103/PhysRevA.106.022615

I. INTRODUCTION

The successful construction of a fully functioning universal quantum computer comes with the promise of allowing us to solve certain computational problems faster (potentially exponentially faster) than with a classical computer. However, the construction of a universal quantum computer comes with its own challenges, i.e., the task to understand the dynamic behavior of quantum systems.

Many experimental prototypes, which aim to realize a universal quantum computer, are based on superconducting circuits. Theoretical descriptions of these systems often use a so-called circuit Hamiltonian model. Here we make a lumped-element approximation (see Sec. 1.4 of Ref. [1]) to derive a Hamiltonian (see, for example, Ref. [2]), which approximately describes the behavior of a particular superconducting circuit.

Unfortunately, it is usually the case that the circuit Hamiltonian model is still too complicated to be treated analytically. Therefore, in most cases additional simplifications are made so that an approximant of the circuit Hamiltonian can be derived. These approximants usually do not come with an estimation of the corresponding approximation error.

In this work we numerically study several instances of such approximants, i.e., effective Hamiltonians, by comparing them to their circuit Hamiltonian counterparts. To this end, we solve the time-dependent Schrödinger equation (TDSE) for both models. This allows us to compare the corresponding solutions and to filter out differences. Furthermore, we also compare the spectra of selected models (see Appendix B).

Since the number of different superconducting circuits is vast, we will focus on three different circuit Hamiltonians and their corresponding effective Hamiltonians. Two of these Hamiltonians are designed to model existing experimental systems (see Refs. [3,4]). Note that for a particular circuit Hamiltonian there might exist a vast amount of different effective models. Considering only systems based on transmon qubits, one might divide the different circuit architectures into two categories: architectures which only use fixed-frequency transmon qubits, an architecture which is primarily studied by IBM, and those using flux-tunable transmon qubits to implement their two-qubit gates. In this work, we focus on circuits which use flux-tunable transmons to implement two-qubit gates. Additionally, we restrict our analysis to systems which only contain one or two qubits, as this suffices to show where the models deviate from each other.

We look at three different systems. The first system is a single flux-tunable transmon. The second system, architecture I, consists of two fixed-frequency transmons, coupled to a flux-tunable transmon. The flux-tunable transmon works as a coupler only [see Fig. 1(a)]. The third system, architecture II, is made up of two flux-tunable transmons, coupled to a transmission line resonator. Here the resonator functions only as a coupler element [see Fig. 1(b)].

This work is structured as follows. In Sec. II A we introduce the different circuit Hamiltonian models for the three systems we simulate in this work. Next, in Sec. II B we derive a nonadiabatic effective Hamiltonian for a single flux-tunable transmon. Then, in Sec. II C, we define two effective two-qubit Hamiltonians, one for architecture I and one for architecture II. The flux-tunable transmons in both these systems are modeled with the adiabatic approximation. In

---

[*] Corresponding author: hannes.a.l@me.com

TABLE I. Device parameters for a tunable coupler architecture, i.e., architecture I. Note that throughout this work we use $\hbar = 1$. The parameter $\omega = E_1 - E_0$ denotes the qubit frequency and $\alpha = (E_2 - E_1) - (E_1 - E_0)$ is the so-called qubit anharmonicity. All parameters are in gigahertz except for the flux offset parameter $\varphi_0 = \varphi(0)$, which is given in units of the flux quantum ϕ_0 [see Eqs. (3) and (33)]. These parameters are motivated by experiments performed by the authors of Ref. [3].

i	$\omega/2\pi$	$\alpha/2\pi$	E_C	$E_{J,1}$	$E_{J,2}$	$\varphi_0/2\pi$	$G_{2,i}/2\pi$
0	5.100	−0.310	6.777	84.482	n/a	n/a	0.085
1	6.200	−0.285	6.453	127.992	n/a	n/a	0.085
2	8.100	−0.235	5.529	112.450	134.999	0.15	n/a

Sec. II D we define a simple control pulse (for the external flux) which allows us to model microwave and unimodal pulses. This pulse (the external flux) enables us to activate resonant and nonadiabatic transitions between the states of the systems we consider. Section III contains the main results of this work. First, in Sec. III A, we study a single flux-tunable transmon. Here we model resonant transitions activated by microwave pulses and nonadiabatic transitions activated by unimodal pulses with the circuit Hamiltonian model and the nonadiabatic effective model we derive in Sec. II B. Here we compare how well both models agree with one another. Next, in Sec. III B, we identify several transitions (interactions) which are suppressed in the effective model for architecture I [see Fig. 1(a)], by the adiabatic approximation we use to model the flux-tunable transmons in the effective two-qubit model. Finally, in Sec. III C, we study two-qubit gate transitions, i.e., transitions which can be used to implement two-qubit gates with the corresponding architectures I and II. For architecture I we use a microwave pulse to activate resonant two-qubit iSWAP and CZ interactions. Similarly, for architecture II we use a unimodal pulse to activate nonadiabatic transitions which allow us to model iSWAP and CZ gates. Here we focus on the often made approximation (see Refs. [3,6–8]) that the effective interaction strength is of static nature. Additionally, we test whether or not nonadiabatic effects play a role. A summary and conclusions drawn from our analysis are presented in Sec. IV.

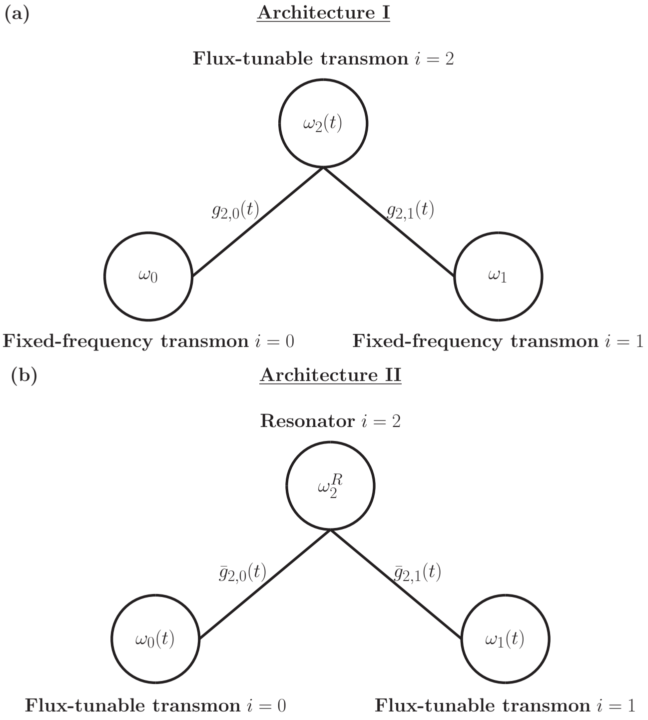

FIG. 1. Sketches of the circuit architectures (a) I and (b) II. Both types of architectures use flux-tunable transmon qubits to activate two-qubit gate transitions (see Ref. [5] for (a) and Ref. [6] for (b)). We use the circuit and effective Hamiltonians given by Eqs. (7) and (31) and the device parameters listed in Tables I and III to perform simulations of iSWAP and CZ two-qubit gate transitions for architecture I. Similarly, we use the circuit and effective Hamiltonians given by Eqs. (8) and (32) and the device parameters listed in Tables II and IV to perform simulations of iSWAP and CZ two-qubit gate transitions for architecture II.

To assist the reader in navigating through the material, we list the main findings:

(1) We provide a derivation of a nonadiabatic effective Hamiltonian for flux-tunable transmons (see Sec. II B). Furthermore, we compare the dynamics of the adiabatic and the nonadiabatic effective model with the ones of the associated circuit model by solving the TDSE for the different model Hamiltonians. This is done for a single flux-tunable transmon (see Sec. III A) and two two-qubit systems [see Figs. 1(a) and 1(b) and Sec. III C].

(2) We identify transitions which are suppressed in the adiabatic effective two-qubit model for the system illustrated in Fig. 1(a) (see Sec. III B).

(3) We show that neglecting nominal small time-dependent oscillations of the interaction strength in an effective model for the two-qubit system shown in Fig. 1(a) can lead to substantial shifts in the duration of a control pulse (see Sec. III C 1). Conversely, we also show that neglecting a nominal much larger time-dependent square-pulse-like reduction of the interaction strength in an effective model for the two-qubit system shown in Fig. 1(b) can lead to modest shifts in the duration of a control pulse (see Sec. III C 2).

II. MODEL

In this section, we introduce the circuit Hamiltonian models (see Sec. II A), we derive effective Hamiltonians for a single fixed-frequency and a single flux-tunable transmon (see Sec. II B), and we discuss effective Hamiltonian models which are commonly used to model two-qubit systems (see Sec. II C). Furthermore, in Sec. II D we define a control pulse which can be used to implement single- and two-qubit gate transitions with an external flux. Note that throughout this work we use $\hbar = 1$.

A. Circuit Hamiltonians

The systems we model in this work consist of two different types of transmons as well as transmission line resonators. The couplings between the different subsystems are modeled as dipole-dipole interactions.

The first type of transmon is the so-called fixed-frequency transmon (see Ref. [9]), described by the circuit Hamiltonian

$$\hat{H}_{\text{Fix}} = E_C \hat{n}^2 - E_J \cos(\hat{\varphi}), \tag{1}$$

where E_C denotes the capacitive energy and E_J is the Josephson energy. The Hamiltonian is defined in terms of the charge $\hat{n}$ and the flux $\hat{\varphi}$ operators. Note that the Hamiltonian in Eq. (1) is often expressed with a factor $4E_C$ instead of E_C. In this work we adopt the convention used in Ref. [10] and not the one of Ref. [9].

The second type of transmon is the flux-tunable transmon. This type of transmon is the main object of our investigation. If the capacitances of both Josephson junctions are equal, we can define the corresponding circuit Hamiltonian which fulfils the irrotational constraint (cf. Refs. [11,12]) as

$$\hat{H}_{\text{Tun}} = E_C \hat{n}^2 - E_{J,1} \cos\left(\hat{\varphi} + \frac{\varphi(t)}{2}\right) - E_{J,2} \cos\left(\hat{\varphi} - \frac{\varphi(t)}{2}\right). \tag{2}$$

This system is characterized by two Josephson energies $E_{J,1}$ and $E_{J,2}$ and another time-dependent variable $\varphi(t)$, which represents an external flux. This external flux is dimensionless,

$$\varphi(t) = \Phi(t)/\phi_0, \tag{3}$$

where $\Phi(t)$ has the dimension of flux and ϕ_0 is the flux quantum. Furthermore, since the Hamiltonian is 2π periodic, $\varphi(t)$ is usually given in units of 2π. We adopt this convention too.

The circuit Hamiltonians in Eqs. (1) and (2) are usually only referred to as transmons if $E_J/E_C \gg 1$ and $(E_{J,1} + E_{J,2})/E_C \gg 1$. Therefore, in this work, we assume that this is true.

Individual transmons can be coupled directly, or indirectly, or both. In this paper, we only consider indirect couplings. This means interactions between individual transmons are conveyed by an additional circuit element, often called a coupler. This coupler can be a transmon itself or a transmission line resonator.

Transmission line resonators are described by the Hamiltonian

$$\hat{H}_{\text{Res}} = \omega^R \hat{a}^\dagger \hat{a}, \tag{4}$$

where ω^R is the resonator frequency. The operators $\hat{a}^\dagger$ and $\hat{a}$ are the bosonic number operators.

We describe the dipole-dipole coupling between two arbitrary transmons i and j by means of the interaction operator

$$\hat{V}_{i,j} = G_{i,j} \hat{n}_i \hat{n}_j, \tag{5}$$

where $G_{i,j}$ is the interaction strength. Similarly, we model the coupling between an arbitrary resonator j and an arbitrary transmon i with the operator

$$\hat{W}_{j,i} = G_{j,i} (\hat{a}^\dagger + \hat{a})_j \hat{n}_i. \tag{6}$$

We can use the different subsystems and the corresponding interaction terms to construct different circuit architectures. In this work, we consider two different architectures, which use flux-tunable transmons to implement the iSWAP and CZ two-qubit gates. Architecture I, which is discussed in Refs. [3,6–8,13], is described by the circuit Hamiltonian

$$\hat{H}_I = \hat{H}_{\text{Fix},0} + \hat{H}_{\text{Fix},1} + \hat{H}_{\text{Tun},2} + \hat{V}_{2,1} + \hat{V}_{2,0}, \tag{7}$$

and architecture II, which is discussed in Refs. [4,14–16], is described by

$$\hat{H}_{II} = \hat{H}_{\text{Tun},0} + \hat{H}_{\text{Tun},1} + H_{\text{Res},2} + \hat{W}_{2,1} + \hat{W}_{2,0}. \tag{8}$$

In the first case, we use a flux-tunable transmon to indirectly couple two fixed-frequency transmons [see Fig. 1(a)]. In the second case, we use a resonator as a coupler between two flux-tunable transmons [see Fig. 1(b)]. The device parameters that we use in our simulations to obtain the results in Sec. III are listed in Table I for architecture I and Table II for architecture II, respectively.

B. From circuit to effective Hamiltonians

In this section, we provide the derivation of a nonadiabatic effective Hamiltonian for flux-tunable transmons. A more detailed discussion, written for readers who are unfamiliar with transmon qubits, is given in Appendix A.

In the case of the fixed-frequency transmon, we use the harmonic basis states

$$\mathcal{B} = \{|m\rangle\}_{m\in\mathbb{N}} \tag{9}$$

to model the dynamics of the system with an effective Hamiltonian. First, we expand the cosine in Eq. (1) to the quartic order. Then, we decompose the term

$$\frac{E_J}{4!}\hat{\varphi}^4 = \frac{E_C}{48}(\hat{D} + \hat{V}) \tag{10}$$

into a part $\hat{D}$ which is diagonal in the basis $\mathcal{B}$ and one $\hat{V}$ which is off diagonal in $\mathcal{B}$. We use the diagonal part to define the Hamiltonian

$$\hat{H}_{\text{fix}} = \omega \hat{b}^\dagger \hat{b} - \frac{E_C}{48}\hat{D}, \tag{11}$$

where $\omega = \sqrt{2E_C E_J}$. Here $\hat{b}^\dagger$ and $\hat{b}$ are the bosonic number operators which can be defined in terms of their action on the basis states $|m\rangle \in \mathcal{B}$. The Hamiltonian can be expressed as

$$\hat{H}_{\text{fix}} = \omega' \hat{b}^\dagger \hat{b} + \frac{\alpha}{2}\hat{b}^\dagger \hat{b}(\hat{b}^\dagger \hat{b} - \hat{I}), \tag{12}$$

where $\omega' = \sqrt{2E_C E_J} + \alpha$ denotes the transmon qubit frequency and $\alpha = -E_C/4$ is referred to as the transmon's anharmonicity. The spectrum of the Hamiltonian in Eq. (12) is in agreement, up to a constant factor, with the results in Appendix C of Ref. [9]. The corresponding results are obtained by means of time-independent perturbation theory. Note that the derivation of Eq. (12) provided in this section is similar but not equivalent to the one presented in Sec. B 4.1.3 of Ref. [17].

For the flux-tunable transmon, one can make use of the fact that the Hamiltonian given by Eq. (2) can be expressed as

$$\hat{H}_{\text{Tun}} = E_C \hat{n}^2 - E_{J,\text{eff}}(t) \cos(\hat{\varphi} - \varphi_{\text{eff}}(t)), \tag{13}$$

TABLE II. Device parameters for architecture II in the same units as the parameters in Table I. These device parameters are motivated by experiments performed by the authors of Ref. [4].

i	$\omega^R/2\pi$	$\omega/2\pi$	$\alpha/2\pi$	E_C	$E_{J,1}$	$E_{J,2}$	$\varphi_0/2\pi$	$G_{2,i}/2\pi$
0	n/a	4.200	−0.320	6.712	19.728	59.184	0	0.300
1	n/a	5.200	−0.295	6.512	30.265	60.529	0	0.300
2	45.000	n/a	n/a	n/a	n/a	n/a	n/a	n/a

with the effective Josephson energy

$$E_{J,\text{eff}}(t) = E_\Sigma \sqrt{\cos\left(\frac{\varphi(t)}{2}\right)^2 + d^2 \sin\left(\frac{\varphi(t)}{2}\right)^2}, \tag{14}$$

and the effective external flux

$$\varphi_{\text{eff}}(t) = \arctan\left(d \tan\left(\frac{\varphi(t)}{2}\right)\right). \tag{15}$$

Here, we introduced the new parameters $E_\Sigma = (E_{J,1} + E_{J,2})$ and $d = (E_{J,2} - E_{J,1})/(E_{J,2} + E_{J,1})$. The latter one is usually referred to as the asymmetry factor (see Ref. [9]).

We want to repeat the quartic-order cosine expansion argumentation that we provided for the fixed-frequency transmon. However, since there is a time dependence in the cosine function in Eq. (13), we need to use the time-dependent harmonic basis states,

$$\mathcal{B}(t) = \{|m(t)\rangle\}_{m\in\mathbb{N}}, \tag{16}$$

to model the dynamics of the system. The TDSE for the state vector,

$$|\Psi^*(t)\rangle = \hat{\mathcal{W}}(t)\,|\Psi(t)\rangle\,, \tag{17}$$

where $\hat{\mathcal{W}}(t)$ denotes the unitary transformation which maps the basis states $\mathcal{B}(0)$ to the basis states $\mathcal{B}(t)$, only stays form invariant, if we use the transformed Hamiltonian

$$\hat{H}^*_{\text{tun}}(t) = \hat{\mathcal{W}}(t)\hat{H}(t)\hat{\mathcal{W}}^\dagger(t) - i\hat{\mathcal{W}}(t)\partial_t\hat{\mathcal{W}}^\dagger(t). \tag{18}$$

Here $\hat{H}(t)$ denotes the fourth-order Hamiltonian which is diagonal in the basis $\mathcal{B}(t)$, i.e., we expand the cosine in Eq. (13) to quartic order and only keep the contributions which are diagonal in the basis $\mathcal{B}(t)$, as for the fixed-frequency transmons in the basis $\mathcal{B}$. Therefore, we can determine the first term in Eq. (18) to be

$$\hat{\mathcal{W}}(t)\hat{H}(t)\hat{\mathcal{W}}^\dagger(t) = \omega'(t)\hat{b}^\dagger\hat{b} + \frac{\alpha}{2}\hat{b}^\dagger\hat{b}(\hat{b}^\dagger\hat{b} - \hat{I}), \tag{19}$$

where $\omega'(t) = \omega(t) + \alpha$ and

$$\omega(t) = \sqrt{2E_C E_\Sigma}\sqrt[4]{\cos\left(\frac{\varphi(t)}{2}\right)^2 + d^2 \sin\left(\frac{\varphi(t)}{2}\right)^2} \tag{20}$$

denotes the tunable frequency.

We can make use of the fact that the harmonic basis states $\mathcal{B}(t)$ can be expressed analytically in the φ space; this enables us to determine the second term in Eq. (18). The result reads

$$\begin{aligned} -i\hat{\mathcal{W}}(t)\partial_t\hat{\mathcal{W}}^\dagger(t) = {} & -i\sqrt{\frac{\xi(t)}{2}}\dot{\varphi}_{\text{eff}}(t)(\hat{b}^\dagger - \hat{b}) \\ & + \frac{i}{4}\frac{\dot{\xi}(t)}{\xi(t)}(\hat{b}^\dagger\hat{b}^\dagger - \hat{b}\hat{b}), \end{aligned} \tag{21}$$

where $\xi(t) = \sqrt{E_{J,\text{eff}}(t)/(2E_C)}$ and we assume that $\xi(t) \neq 0$ for all times t. Additionally, we find

$$\dot{\varphi}_{\text{eff}}(t) = \dot{\varphi}(t)\frac{d}{2\left(\cos\left(\frac{\varphi(t)}{2}\right)^2 + d^2\sin\left(\frac{\varphi(t)}{2}\right)^2\right)} \tag{22}$$

and

$$\frac{\dot{\xi}(t)}{\xi(t)} = \dot{\varphi}(t)\frac{(d^2-1)\sin(\varphi(t))}{8\left(\cos\left(\frac{\varphi(t)}{2}\right)^2 + d^2\sin\left(\frac{\varphi(t)}{2}\right)^2\right)}, \tag{23}$$

so that the first (second) drive term in Eq. (21) disappears if $d = 0$ ($d = 1$). Consequently, we see that both drive terms in Eq. (21) are not necessarily periodic in $\varphi(t)$ [see the factor $\dot{\varphi}(t)$].

So far we did not discuss whether or not it is justified to drop the higher-order terms in the cosine expansion. We investigate this question in Sec. III A; i.e., we compare the results for the effective Hamiltonian model with the ones of the circuit Hamiltonian model by solving the TDSE for both Hamiltonians numerically.

C. Effective Hamiltonians

The circuit Hamiltonian in Eq. (1) for a fixed-frequency transmon was analytically discussed by the authors of Ref. [9]. This work motivated several studies (see, for example, Refs. [3,6,8,14,15,18]), where fixed-frequency and/or flux-tunable transmons are modeled as anharmonic oscillators with fixed or tunable frequencies.

In practice, only a few basis states are used to model the dynamics of a transmon. Furthermore, presumably for simplicity one often uses a simpler choice for the parametrization of the model. For the fixed-frequency transmon the corresponding effective Hamiltonian can be expressed as

$$\hat{H}_{\text{fix}} = \sum_{m=0,1,2,3}\left(m\omega + \frac{\alpha}{2}m(m-1)\right)|m\rangle\langle m|\,, \tag{24}$$

where the qubit frequency $\omega = (E^{(1)} - E^{(0)})$ and anharmonicity $\alpha = (E^{(2)} - E^{(0)}) - 2\omega$ might be directly fitted to the first and second energy gaps. Obviously, this approach is preferable when detailed knowledge of the capacitive and Josephson energies is not available.

Similarly, in practice flux-tunable transmons are often modeled with the effective Hamiltonian

$$\hat{H}_{\text{tun}}(t) = \sum_{m=0,1,2,3}\left(m\omega(t) + \frac{\alpha}{2}m(m-1)\right)|m\rangle\langle m|\,, \tag{25}$$

where $\omega(t)$ is given by Eq. (20). In this model, the parameters $\omega(0)$, α, and d are used to characterize the flux-tunable transmon qubit. We emphasize that using the tunable frequency given by Eq. (20) to approximate the spectrum of the circuit Hamiltonian in Eq. (2) does not always lead to accurate results. We explore this issue in Appendix B.

The Hamiltonian in Eq. (25) is often stated with reference to Ref. [9] but there is no mentioning of nonadiabatic effects (see, for example, Refs. [6–8,18,19]). Furthermore, note that in Eq. (25) the time dependence of the basis states is not made explicit; this seems to be common practice when working with this model. We simply state the Hamiltonian in Eq. (25) and do not advocate its use. In fact, we are interested in the question to what extent this effective Hamiltonian deviates from its circuit Hamiltonian counterpart in Eq. (2) and the effective Hamiltonian given by Eq. (18) (see Sec. III A).

The Hamiltonian in Eq. (25) is so simple that we can determine the formal solution of the TDSE for all pulses $\varphi(t)$. If we initialize the system in some arbitrary state

$$|\Psi^{\text{tun}}(t_0)\rangle = \sum_{m=0,1,2,3} c_m(t_0)\,|m\rangle\,, \tag{26}$$

we obtain

$$|\Psi^{\text{tun}}(t)\rangle = \sum_{m=0,1,2,3} e^{-i\int_{t_0}^{t} E^{(m)}(t')dt'} c_m(t_0)\,|m\rangle \tag{27}$$

as the formal solution of the TDSE. As one can see, the state population cannot change, no matter how we modulate the external flux $\varphi(t)$.

In Sec. II B, we derive the model of a time-dependent anharmonic oscillator [see Eqs. (18)–(21)]. Here we find that the nonadiabatic drive term in Eq. (21) is proportional to the derivative $\dot{\varphi}(t)$ of the external flux. Consequently, the Hamiltonian in Eq. (25) can generate the correct dynamics if the external flux is varied sufficiently slowly such that $\dot{\varphi}(t) \rightarrow 0$ and the system is described in a time-dependent basis [see Eqs. (17) and (18)]. Note that this result is in agreement with the adiabatic theorem (see Refs. [20,21]).

The model Hamiltonian for the transmission line resonator given by Eq. (4) is already diagonal in the harmonic basis. Therefore, no further approximations are necessary. However, if we intend to derive effective Hamiltonians for the circuit Hamiltonians in Eqs. (7) and (8), we also have to consider the interaction operators. This means we have to replace the charge operator $\hat{n}$ by an effective operator $\hat{n}_{\text{eff}}$. In this work we use the operator

$$\hat{n}_{\text{eff}} = \sqrt[4]{\frac{E_J}{8E_C}} \sum_{m=0,1,2,3} \sqrt{m+1}(|m\rangle\langle m+1| + |m+1\rangle\langle m|), \tag{28}$$

which was also discussed in Ref. [9]. If we couple flux-tunable transmons, we perform the substitution $E_J \rightarrow E_{J\text{eff}}(t)$. The effective interaction strength for a coupling between a fixed-frequency transmon i and a flux-tunable transmon j is given by

$$g_{j,i}(t) = G_{j,i}\sqrt[4]{\frac{E_{J_j\text{eff}}(t)}{8E_{C_j}}}\sqrt[4]{\frac{E_{J_i}}{8E_{C_i}}}, \tag{29}$$

where $G_{j,i}$ is the original coupling strength [see Eqs. (5) and (6)]. Similarly, the effective interaction strength, between a resonator j and a flux-tunable transmon i, reads

$$\bar{g}_{j,i}(t) = G_{j,i}\sqrt[4]{\frac{E_{J_i\text{eff}}(t)}{8E_{C_i}}}. \tag{30}$$

We find that the effective interaction strength is now time dependent. Note that this time dependence is frequently neglected (see Refs. [3,3,6–8,19,22]).

TABLE III. Parameters for an effective Hamiltonian model of architecture I. See Table I and Eq. (7) for details and units.

i	$\omega/2\pi$	$\alpha/2\pi$	$\varphi_0/2\pi$	$g_{2,i}(\varphi_0)/2\pi$
0	5.100	−0.310	n/a	0.146
1	6.200	−0.285	n/a	0.164
2	8.100	−0.235	0.15	n/a

It is often the case that the complete effective Hamiltonian is expressed solely in terms of bosonic number operators. In this representation the effective model Hamiltonian for architecture I reads

$$\begin{aligned}\hat{H}_I^{\text{eff}} &= \omega_0\hat{b}_0^\dagger\hat{b}_0 + \frac{\alpha_0}{2}\hat{b}_0^\dagger\hat{b}_0(\hat{b}_0^\dagger\hat{b}_0 - \hat{I})\\ &+ \omega_1\hat{b}_1^\dagger\hat{b}_1 + \frac{\alpha_1}{2}\hat{b}_1^\dagger\hat{b}_1(\hat{b}_1^\dagger\hat{b}_1 - \hat{I})\\ &+ \omega_2(t)\hat{b}_2^\dagger\hat{b}_2 + \frac{\alpha_2}{2}\hat{b}_2^\dagger\hat{b}_2(\hat{b}_2^\dagger\hat{b}_2 - \hat{I})\\ &+ g_{2,1}(t)(\hat{b}_2^\dagger + \hat{b}_2)(\hat{b}_1^\dagger + \hat{b}_1)\\ &+ g_{2,0}(t)(\hat{b}_2^\dagger + \hat{b}_2)(\hat{b}_0^\dagger + \hat{b}_0).\end{aligned} \tag{31}$$

Similarly, the effective model Hamiltonian for architecture II can be expressed as

$$\begin{aligned}\hat{H}_{II}^{\text{eff}} &= \omega_0(t)\hat{b}_0^\dagger\hat{b}_0 + \frac{\alpha_0}{2}\hat{b}_0^\dagger\hat{b}_0(\hat{b}_0^\dagger\hat{b}_0 - \hat{I})\\ &+ \omega_1(t)\hat{b}_1^\dagger\hat{b}_1 + \frac{\alpha_1}{2}\hat{b}_1^\dagger\hat{b}_1(\hat{b}_1^\dagger\hat{b}_1 - \hat{I})\\ &+ \omega_2^R\hat{a}_2^\dagger\hat{a}_2\\ &+ \bar{g}_{2,1}(t)(\hat{a}_2^\dagger + \hat{a}_2)(\hat{b}_1^\dagger + \hat{b}_1)\\ &+ \bar{g}_{2,0}(t)(\hat{a}_2^\dagger + \hat{a}_2)(\hat{b}_0^\dagger + \hat{b}_0).\end{aligned} \tag{32}$$

The device parameters that we use in our simulations to obtain the results in Sec. III are listed in Table III for architecture I and Table IV for architecture II, respectively. Note that the Hamiltonians in Eqs. (31) and (32) both lack the drive term given by Eq. (21). Consequently, here we model the flux-tunable transmons adiabatically. In Secs. III B and III C we simulate both Hamiltonians with and without the drive term and compare the results.

TABLE IV. Parameters for an effective Hamiltonian model of architecture II. See Table II and Eq. (8) for details and units.

i	$\omega^R/2\pi$	$\omega/2\pi$	$\alpha/2\pi$	$\varphi_0/2\pi$	$g_{2,i}(\varphi_0)/2\pi$
0	n/a	4.200	−0.320	0	0.307
1	n/a	5.200	−0.295	0	0.344
2	45.000	n/a	n/a	n/a	n/a

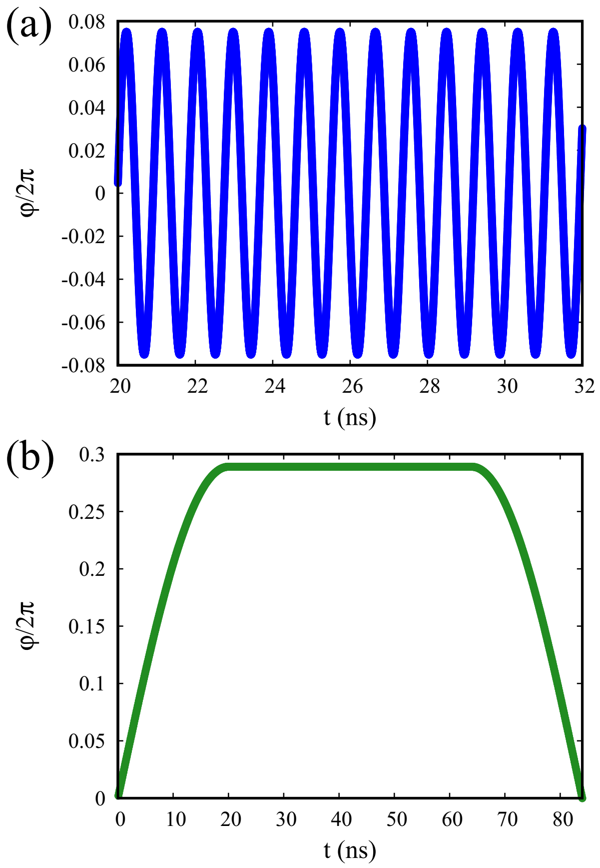

FIG. 2. External flux $\varphi/2\pi$ as a function of time for two different flux control pulses. (a) Microwave pulse using Eq. (33), amplitude $\delta/2\pi = 0.075$, drive frequency $\omega^D/2\pi = 1.089$ GHz, a rise and fall time of $T_{\mathrm{r/f}} = 13$ ns, and pulse duration $T_{\mathrm{d}} = 205.4$ ns. (b) Unimodal pulse using Eq. (33), amplitude $\delta/2\pi = 0.297$, drive frequency $\omega^D/2\pi = 0$ GHz, a rise and fall time of $T_{\mathrm{r/f}} = 20$ ns, and pulse duration $T_{\mathrm{d}} = 84$ ns.

D. Control pulse

All simulations in this work are performed with a control pulse (external flux) of the form

$$\varphi(t) = \varphi_0 + \delta e(t) \cos(\omega^D t), \tag{33}$$

where the real-valued parameters φ_0, δ, and ω^D denote the flux offset, the pulse amplitude, and the drive frequency, respectively. The envelope function $e(t)$ is taken to be of the form

$$e(t) = \begin{cases} \sin(\lambda t) & \text{if } 0 \leqslant t < T_{\mathrm{r/f}} \\ 1 & \text{if } T_{\mathrm{r/f}} \leqslant t \leqslant \Delta T \\ \sin(\frac{\pi}{2} + \lambda(t - \Delta T)) & \text{if } \Delta T < t \leqslant T_{\mathrm{d}}. \end{cases} \tag{34}$$

Here $T_{\mathrm{r/f}}$ denotes the rise and fall time, T_{d} is the control pulse duration, and $\Delta T = (T_{\mathrm{d}} - T_{\mathrm{r/f}})$. The parameter $\lambda = \pi/(2T_{\mathrm{r/f}})$ is determined by the rise and fall time. This generic flux pulse allows us to control various transitions between states of the systems.

Figures 2(a) and 2(b) show the external flux $\varphi/2\pi$ as functions of time t for the two different types of flux control pulses we use in this work. Figure 2(a) shows a microwave pulse. Here we use Eq. (33), the amplitude $\delta/2\pi = 0.075$, the drive frequency $\omega^D/2\pi = 1.089$ GHz, a rise and fall time $T_{\mathrm{r/f}} = 13$ ns, and the pulse duration $T_{\mathrm{d}} = 205.4$ ns. This type of control pulse is used for architecture I. Figure 2(b) shows a unimodal pulse. Here we use Eq. (33), the amplitude $\delta/2\pi = 0.297$, the drive frequency $\omega^D/2\pi = 0$ GHz, a rise and fall time $T_{\mathrm{r/f}} = 20$ ns, and the pulse duration $T_{\mathrm{d}} = 84$ ns. This type of control pulse is used to implement nonadiabatic gates (see Ref. [5]) with architecture II.

III. RESULTS

In this section we present our findings. First, in Sec. III A, we consider a single flux-tunable transmon. Here we focus on the transition dynamics and compare the effective Hamiltonians in Eqs. (18) and (25) with the circuit Hamiltonian given by Eq. (2). Next, in Sec. III B, we identify transitions (interactions) which seem to be suppressed in the effective model of architecture I given by Eq. (31). Finally, in Sec. III C, we study how different approximations affect the unsuppressed transitions which are often used to implement two-qubit gates with architectures I and II.

A detailed discussion of the simulation results for the circuit Hamiltonian (where we do not make approximations to solve the TDSE) is provided in Appendix D. A summary of the simulation results for the circuit Hamiltonian can be found in Table VI. Here we use the device parameters listed in Table I (Table II) to obtain the results for architecture I (architecture II). In the following sections we compare these results with the ones we obtain by simulating the effective models. A summary of the results for the effective models can be found in Table VII. Appendix C introduces the simulation algorithm we use to obtain the results in this section. Note that throughout this work we use $\hbar = 1$.

A. Simulations of a single flux-tunable transmon

In this section, we compare the pulse response of the circuit Hamiltonian given by Eq. (2) with the one of the effective Hamiltonians in Eqs. (18) and (25). Note that we do not need to simulate the effective Hamiltonian given by Eq. (25). The formal solution of its TDSE is given by Eq. (27) in Sec. II C.

For the simulations in this section we use the device parameters listed in Table I, row $i = 2$, and the pulse $\varphi(t)$ in Eq. (33). We consider two cases. First, we consider resonant transitions driven by a microwave pulse [see Fig. 2(a)], whose drive frequency ω^D coincides with the energy gap $E^{(1)} - E^{(0)}$ of the flux-tunable transmon system. The results are presented in Figs. 3(a) and 3(b) and Figs. 4(a) and 4(b). Second, we consider nonadiabatic transitions driven by a unimodal pulse [see Fig. 2(b)] with the drive frequency $\omega^D = 0$. The corresponding results are displayed in Figs. 5(a)–5(h).

Figures 3(a) and 3(b) show the ground-state probabilities $p^{(0)}$ as functions of the pulse duration T_{d} and the drive frequency ω^D. We use the pulse amplitude $\delta/2\pi = 0.001$ and the rise and fall time $T_{\mathrm{r/f}} = T_{\mathrm{d}}/2$ to obtain the results. For Fig. 3(a) we solve the TDSE for the circuit Hamiltonian given by Eq. (2) and center the results around the transition frequency $\omega^{(0)} = 7.636$ GHz. Similarly, for Fig. 3(b) we solve the TDSE for the effective Hamiltonian in Eq. (18) and center the results around the transition frequency $\omega^{(0)} = 7.643$ GHz.

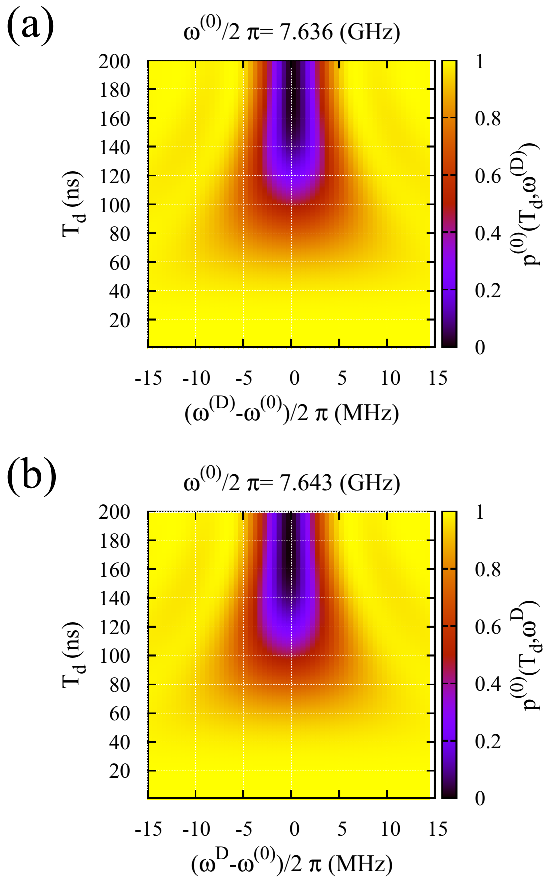

FIG. 3. Ground-state probabilities $p^{(0)}$ as functions of the pulse duration T_{d} and the drive frequency ω^D. We use the device parameters for a single flux-tunable transmon listed in Table I, row $i=2$, and the pulse given by Eq. (33) with $T_{\mathrm{r/f}}=T_{\mathrm{d}}/2$ and the pulse amplitude $\delta/2\pi=0.001$ [see Fig. 2(a)] to obtain the results. The results in (a) are obtained by solving the TDSE for the circuit Hamiltonian in Eq. (2). Similarly, the results in (b) are obtained by solving the TDSE for the nonadiabatic effective Hamiltonian in Eq. (18). At time $t=0$ the systems are initialized in the corresponding eigenstates $p^{(0)}(0)=1$. Here we model Rabi transitions between the ground state and the first excited state. Note that (a) and (b) are centered around the frequency $\omega^{(0)}$ which corresponds to the energy difference $E^{(1)}-E^{(0)}$ in the corresponding model, i.e., the circuit or the effective model. We see that apart from the shift in the transition frequency both models show a similar qualitative and quantitative behavior. However, the effective model given by the Hamiltonian in Eq. (25) does not allow us to model these transitions.

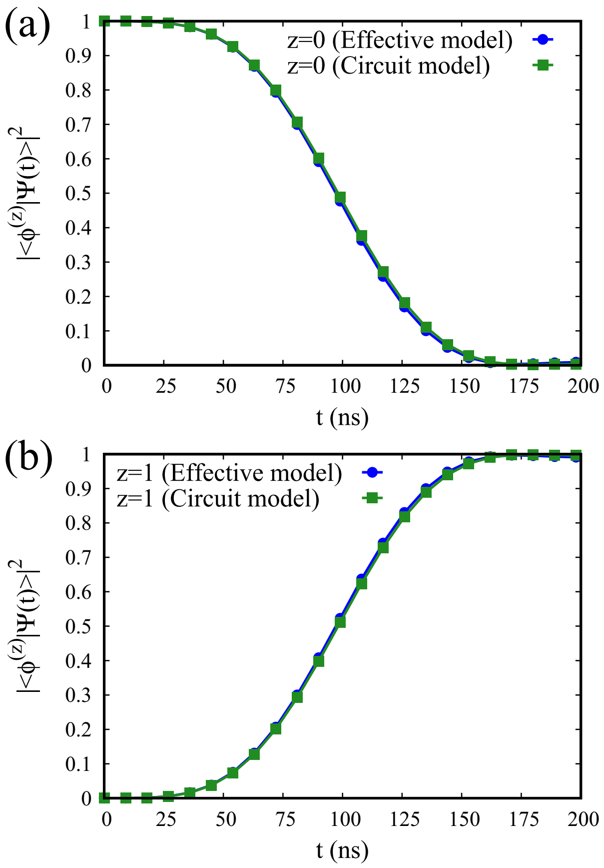

FIG. 4. Probabilities (a) $p^{(0)}(t)$ and (b) $p^{(1)}(t)$ as functions of time t obtained with the effective model (blue circles) and the circuit model (green squares). We use the pulse given by Eq. (33) with the pulse amplitude $\delta/2\pi=0.001$, the pulse duration $T_{\mathrm{d}}=200\,\mathrm{ns}$, the rise and fall time $T_{\mathrm{r/f}}=100\,\mathrm{ns}$, and the device parameters for a single flux-tunable transmon listed in Table I, row $i=2$, to obtain the results. We use the drive frequency $\omega^D=7.636\,\mathrm{GHz}$ to obtain the results with the circuit Hamiltonian, Eq. (2). Similarly, we use the drive frequency $\omega^D=7.643\,\mathrm{GHz}$ to obtain the results with the effective Hamiltonian, Eq. (18). The systems are initialized in the ground state $p^{(0)}=1$ at time $t=0$. Note that in (a) and (b) we use the frequencies which cut through the centers of the chevron patterns in Figs. 3(a) and 3(b). As one can see, (a) and (b) show qualitatively and quantitatively similar behavior with respect to the time evolution.

The 7 MHz difference in terms of the transition frequency stems from the fact that the fourth-order expansion does not lead to the exact same spectrum.

We also simulated the effective model given by Eq. (18) with higher-order terms (data not shown) (see Sec. II B). Here we find that the chevron pattern in Fig. 3(b) stays the same but the transition frequency changes due to the higher-order terms. If we add enough terms to the cosine expansion, the results converge. Note that we simulated the model up to 60th order.

Furthermore, in Appendix B we numerically investigate how well the spectrum of the circuit Hamiltonian can be approximated by the tunable frequency given by Eq. (20). We find that the deviations increase with the flux $\varphi/2\pi\rightarrow 0.5$. For the fourth-order expansion and the operating point $\varphi_0/2\pi=0.15$, deviations of the order of 10 MHz are characteristic.

Clearly, the results in Figs. 3(a) and 3(b) show a similar qualitative and quantitative behavior. Furthermore, Figs. 4(a) and 4(b) show the time evolution of the probabilities $p^{(0)}(t)$ and, respectively, obtained with the effective and the circuit model. Here we use the frequencies which cut through the centers of the chevron patterns in Figs. 3(a) and 3(b) and add the data for the first excited state $p^{(1)}(t)$ [see Fig. 4(b)]. One can observe that the time evolutions of the probabilities are qualitatively and quantitatively very similar.

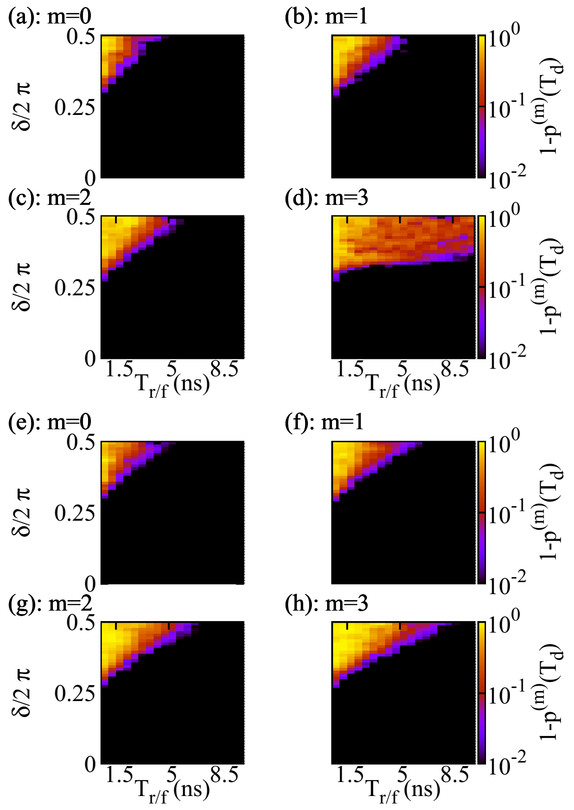

FIG. 5. Probabilities $1 - p^{(m)}$ at time T_d as functions of the rise and fall time $T_{\mathrm{r/f}}$ and the pulse amplitude δ. We use the pulse given by Eq. (33) with $\omega^D = 0$ GHz and $T_{\mathrm{d}} = 50$ ns [see Fig. 2(b)] and the device parameters for a single flux-tunable transmon listed in Table I, row $i = 2$, to obtain the results. The results for (a) $m = 0$, (b) $m = 1$, (c) $m = 2$, and (d) $m = 3$ are obtained by solving the TDSE for the circuit Hamiltonian in Eq. (2). Similarly, the results for (e) $m = 0$, (f) $m = 1$, (g) $m = 2$, and (h) $m = 3$ are obtained by solving the TDSE for the nonadiabatic effective Hamiltonian given by Eq. (18). At time $t = 0$ the systems are initialized in the corresponding eigenstates $p^{(m)}(0) = 1$. The simulations test whether or not we have left the pulse parameter regime where the adiabatic approximation is valid; i.e., the bright areas indicate the parameters which lead to nonadiabatic transitions. Note that it is impossible to use the effective Hamiltonian in Eq. (25) to model such nonadiabatic transitions. Interestingly, for $m = 0$, $m = 1$, and $m = 2$ the effective model given by the Hamiltonian in Eq. (18) shows a qualitatively similar behavior as the circuit model by the Hamiltonian in Eq. (2).

The time evolution of the effective Hamiltonian given by Eq. (25) for this scenario is trivial; i.e., the system simply remains in its initial state.

We now consider the second case, i.e., nonadiabatic transitions driven by a unimodal pulse. Figures 5(a)–5(h) show the probabilities $1 - p^{(m)}$ at time T_{d} as functions of the rise and fall time $T_{\mathrm{r/f}}$ and the pulse amplitude δ. We use a unimodal pulse [see Fig. 2(b)] with $\omega^D = 0$ and $T_{\mathrm{d}} = 50$ ns to obtain the results. In Figs. 5(a)–5(d) we use the circuit Hamiltonian given by Eq. (2) to obtain the results for $m = 0, m = 1, m = 2$, and $m = 3$, respectively. Similarly, in Figs. 5(e)–5(h) we use the effective Hamiltonian given by Eq. (18) to obtain the results for $m = 0$, $m = 1$, $m = 2$, and $m = 3$, respectively. At time $t = 0$ we initialize the system in the corresponding eigenstates, i.e., $p^{(m)}(0) = 1$. Therefore, the simulations test whether or not the pulse parameters are still in the regime where the adiabatic approximation (see Refs. [20,21]) is valid. The bright areas correspond to pulse parameters which induce nonadiabatic transitions.

As one can see, the circuit model given by Eq. (2) and the effective model in Eq. (18) yield qualitative similar results for $m = 0$, $m = 1$, and $m = 2$. The results for $m = 3$ deviate qualitatively and quantitatively.

As before, the time evolution of the effective Hamiltonian given by Eq. (25) for this scenario is trivial; i.e., the system simply remains in its initial state such that $1 - p^{(m)}(t) = 0$ for all $m \in \{0, 1, 2, 3\}$ and time t.

In summary, the effective flux-tunable Hamiltonian given by Eq. (25) cannot describe any of the transitions we can model with the Hamiltonians in Eqs. (2) and (18). Furthermore, we presented results which show that the effective flux-tunable Hamiltonian given by Eq. (18) and the circuit Hamiltonian given by Eq. (2) generate qualitative and sometimes even quantitative similar pulse responses; see Figs. 3(a) and 3(b) and Figs. 4(a) and 4(b) for the case of resonant transitions and Figs. 5(a)–5(h) for the case of nonadiabatic transitions. Some of the deviations we find, e.g., small shifts in the transition frequency, might be explained by the fact that the spectrum of the effective model given by Eq. (18) is not exactly the one of the circuit model given by Eq. (2). Furthermore, additional deviations might be attributed to the fact that we truncate the cosine expansion up to a finite order [see the Hamiltonian in Eq. (13) and Sec. II B]. The full dynamic behavior, with regard to the circuit model, might only be recovered if we include all terms.

B. Simulations of suppressed transitions in the effective two-qubit model

In the previous section, we discussed the case of a single flux-tunable transmon. In this section we consider transitions in a two-qubit system which are suppressed in the effective model. Here we use the effective model Hamiltonian in Eq. (31) and the parameters listed in Table III to obtain the results. The effective Hamiltonian describes a two-qubit system (two qubits and one coupler). We index the different states by using tuples of the form $z = (k_0, m_1, m_0)$, where $k_0 \in \{0, 1, 2, 3\}$ is the coupler index, $m_1 \in \{0, 1, 2, 3\}$ is the index of the second qubit, and $m_0 \in \{0, 1, 2, 3\}$ is the index of the first qubit. Previous work by the authors of Refs. [3,6,7] shows that at least the transitions $z = (0, 0, 1) \rightarrow z = (0, 1, 0)$ and $z = (0, 1, 1) \rightarrow z = (0, 2, 0)$ can be activated by modulating the coupler frequency given by Eq. (20) with a microwave pulse (see also Sec. III C).

Our aim is to model the transitions $z = (0, 0, 0) \rightarrow z = (0, 1, 0)$ and $z = (0, 0, 0) \rightarrow z = (0, 0, 1)$ for a two-qubit system. We are able to model these transitions with the circuit Hamiltonian in Eq. (7) and the device parameters listed in Table I (the pulse parameters are summarized in Table VI). However, we find that the effective model does not respond to pulses of the form of Eq. (33), with pulse parameters similar to the ones given in Table VI. Therefore, we search for the corresponding transitions in a more systematic way. We initialize

TABLE V. Results of the computation of the function $\epsilon = 1 - \min_{(\omega^D,\delta,t)\in\mathcal{G}}(p^{(0,0,0)}(\omega^D,\delta,t))$. Here ω^D denotes the drive frequency and δ is the pulse amplitude. The initial state of the system is $|\phi^{(0,0,0)}\rangle$ in all cases. The probability $p^{(0,0,0)}(\omega^D,\delta,t) = |\langle\phi^{(0,0,0)}|\Psi(\omega^D,\delta,t)\rangle|^2$ is determined for various pulses and points in time so that the minimum can be obtained. The first three columns show the search intervals for ω^D, δ, and T_d, which define the search grid $(\omega^D,\delta,t)\in\mathcal{G}\subseteq\mathbb{R}^3$. The step parameters are set to $\Delta\omega/2\pi = 10^{-5}$ GHz, $\Delta\delta/2\pi = 10^{-3}$, and $\Delta t = 0.2$ ns. The last column shows the result for ϵ. The results are obtained with the system parameters listed in Table III and the effective Hamiltonian in Eq. (31).

$\omega^D/2\pi$	$\delta/2\pi$	T_d	ϵ
[4.90,5.30]	[0.000,0.110]	[0,300]	10^{-3}
[6.00,6.40]	[0.000,0.110]	[0,300]	10^{-3}
[0.00,0.00]	[0.000,0.000]	[0,300]	10^{-3}

the system in the state $z = (0,0,0)$ and compute the probability $p^{(0,0,0)}(\omega^D,\delta,t) = |\langle\phi^{(0,0,0)}|\Psi(\omega^{\mathrm{D}},\delta,t)\rangle|^2$ for various control pulses, which are characterized by the drive frequency ω^{D} and the amplitude δ. This allows us to determine the value of the indicator

$$\epsilon = 1 - \min_{(\omega^D,\delta,t)\in\mathcal{G}}(p^{(0,0,0)}(\omega^D,\delta,t)), \tag{35}$$

where $\mathcal{G}\subseteq\mathbb{R}^3$ denotes a grid which ranges over a discrete set of pulse parameters and a discrete set of points in time.

Every row in Table V corresponds to a different search grid. In the first row we search for an excitation of the first qubit. This means we have to consider the frequency range [4.90,5.30]. Similarly, in the second row we search in the frequency range [6.00,6.40]. The last row serves as a reference. Here we simulate the free time evolution; i.e., we do not apply any external flux to the system. Since we do not want to activate transitions by accidentally creating an avoided crossing between different energies, we restrict the search range of the amplitude to $\delta/2\pi \in [0.000, 0.110]$. The step parameters are set to $\Delta\omega/2\pi = 10^{-5}$ GHz, $\Delta t = 0.2$ ns, and $\Delta\delta/2\pi = 10^{-3}$. In all cases we find that $\epsilon \approx 0.001$. This means that the free time evolution yields the same result as the instances where we compute ϵ for cases where we apply pulses. The results suggest that the system reacts to these sets of pulses in the same way it does to no pulse at all; i.e., the system remains mainly in its ground state.

Figures 6(a) and 6(b) show two chevron patterns obtained for the circuit Hamiltonian in Eq. (7). We used these figures to determine the pulse parameters for the results we presented in Table VI (see rows 3 and 4). The chevron patterns in Figs. 6(a) and 6(b) are several megahertz wide. Therefore, assuming that the effective Hamiltonian in Eq. (31) allows us to model these operations, we would expect that $\epsilon \approx 1.000$. However, since this is not the case, we might conclude that we cannot model these transitions with the Hamiltonian in Eq. (31). Note that these results are in accordance with the single flux-tunable transmon case. Furthermore, there are other transitions, e.g., $z = (0,0,0) \rightarrow z = (1,0,0)$, which seem to be suppressed. Therefore, our listing is not complete.

The deficit of the effective model Hamiltonian that it does not describe all the transitions might become relevant once we consider more and more qubits in one system, i.e., if we consider the spectral crowding problem.

We also simulated the effective model given by Eq. (31) with an additional nonadiabatic drive term given by Eq. (21), for the flux-tunable coupler. Here we find (data not shown) that one can model the transitions $z = (0,0,0) \rightarrow z = (0,1,0)$, $z = (0,0,0) \rightarrow z = (0,0,1)$, and others with the nonadiabatic effective model. The nonadiabatic effective model shows a similar response [see Figs. 6(a) and 6(b)] as the circuit Hamiltonian given by Eq. (7).

C. Simulation of unsuppressed transitions in the effective two-qubit model

It is common practice (see Refs. [3,3,6–8,19,22]) that multiqubit Hamiltonians are simplified by making assumptions about the effective parameters which influence the dynamics of the system. We begin this section with a discussion of one of these assumptions, namely, that the effective interaction strength g [see Eqs. (31) and (32)] between the different subsystems is time independent.

Figures 7(a) and 7(b) show the effective interaction strengths g (in blue on the left y axis) for architecture I and $\bar{g}$ (in green on the right y axis) for architecture II as functions of the external flux $\varphi/2\pi$. The values for $g(\varphi)$ were determined with Eq. (29) and the parameters listed in Table I, row $i = 2$.

TABLE VI. Summary of all model and pulse parameters used to perform simulations of the circuit Hamiltonians in Eqs. (2), (7), and (8) (see Appendix D). The first column lists the model Hamiltonian and the system parameters (in the form of references). The second column states which gate is modeled. The third column gives the states which are being controlled. The next columns show the following pulse parameters: the drive frequency $\omega^D/2\pi$ (GHz), the amplitude $\delta/2\pi$ in units of the flux quantum ϕ_0, the rise and fall time $T_{\mathrm{r/f}}$ (ns), and the gate duration T_{d} (ns). The last column shows the number of basis states, N_m, which are needed to obtain an accurate solution.

Hamiltonian and parameters	Gate	States z	$\omega^D/2\pi$	$\delta/2\pi$	$T_{\mathrm{r/f}}$	T_{d}	N_m
Eq. (2) and Table I	X	$\{(0),(1)\}$	7.636	0.001	10	20	3
Eq. (2) and Table I	X	$\{(0),(1)\}$	7.636	0.01	100	200	3
Eq. (7) and Table I	X	$\{(0,0,0),(0,1,0)\}$	6.183	0.045	22.5	45	3
Eq. (7) and Table I	X	$\{(0,0,0),(0,0,1)\}$	5.092	0.085	25	50	3
Eq. (7) and Table I	iSWAP	$\{(0,1,0),(0,0,1)\}$	1.089	0.075	13	209.40	6
Eq. (7) and Table I	CZ	$\{(0,1,1),(0,2,0)\}$	0.809	0.085	13	297.55	8
Eq. (8) and Table II	iSWAP	$\{(0,1,0),(0,0,1)\}$	0	0.289	20	100	14
Eq. (8) and Table II	CZ	$\{(0,1,1),(0,0,2)\}$	0	0.3335	20	125	16

TABLE VII. Summary of all pulse parameters we use to perform the simulations of the effective models in Eqs. (18), (25), (31), and (32). The first column lists the model Hamiltonian and the system parameters (in the form of references). The second column shows which case we simulate. In case A we use a static interaction strength and a nonadjusted spectrum to model the system. In case B we use a time-dependent interaction and a nonadjusted spectrum to obtain the results. Similarly, in case C we use a time-dependent interaction strength and an adjusted spectrum. The third column displays the figure which contains the results. The fourth column states which gate we model. The fifth column shows the states which are being controlled. The next columns show the following pulse parameters: the drive frequency $\omega^D/2\pi$ (GHz), the amplitude $\delta/2\pi$ in units of the flux quantum ϕ_0, the rise and fall time $T_{\mathrm{r/f}}$ (ns), and the gate duration T_{d} (ns). In the last column we state whether or not is was possible to model the gate (see Sec. III B for more details). If it is not possible to model a transition, we label the corresponding parameters with not applicable (n/a).

Hamiltonian and parameters	Case	Fig.	Gate	States z	$\omega^D/2\pi$	$\delta/2\pi$	$T_{\mathrm{r/f}}$	T_{d}	Can be modeled?
Eq. (18) and Table I	n/a	n/a	X	$\{(0), (1)\}$	7.643	0.01	10	20	Yes
Eq. (18) and Table I	n/a	Fig. 4(b)	X	$\{(0), (1)\}$	7.643	0.001	100	200	Yes
Eq. (25) and Table III	n/a	n/a	X	$\{(0), (1)\}$	n/a	n/a	n/a	n/a	No
Eq. (25) and Table III	n/a	n/a	X	$\{(0), (1)\}$	n/a	n/a	n/a	n/a	No
Eq. (31) and Table III	n/a	n/a	X	$\{(0, 0, 0), (0, 1, 0)\}$	n/a	n/a	n/a	n/a	No
Eq. (31) and Table III	n/a	n/a	X	$\{(0, 0, 0), (0, 0, 1)\}$	n/a	n/a	n/a	n/a	No
Eq. (31) and Table III	A	Fig. 9(a)	iSWAP	$\{(0, 1, 0), (0, 0, 1)\}$	1.088	0.075	13	139.6	Yes
Eq. (31) and Table I	B	Fig. 9(b)	iSWAP	$\{(0, 1, 0), (0, 0, 1)\}$	1.089	0.075	13	205.4	Yes
Eq. (31) and Table III	A	Fig. 9(c)	CZ	$\{(0, 1, 1), (0, 2, 0)\}$	0.807	0.085	13	196.5	Yes
Eq. (31) and Table I	B	Fig. 9(d)	CZ	$\{(0, 1, 1), (0, 2, 0)\}$	0.807	0.085	13	272.00	Yes
Eq. (32) and Table IV	A	Fig. 12(a)	iSWAP	$\{(0, 1, 0), (0, 0, 1)\}$	0	0.297	20	84	Yes
Eq. (32) and Table II	C	Fig. 12(b)	iSWAP	$\{(0, 1, 0), (0, 0, 1)\}$	0	0.289	20	96	Yes
Eq. (32) and Table IV	A	Fig. 12(c)	CZ	$\{(0, 1, 1), (0, 0, 2)\}$	0	0.343	20	105	Yes
Eq. (32) and Table II	C	Fig. 12(d)	CZ	$\{(0, 1, 1), (0, 0, 2)\}$	0	0.334	20	121	Yes

Similarly, the values for $\bar{g}(\varphi)$ are obtained with the parameters listed in Table II, row $i = 1$, and Eq. (30). We can see that both effective interaction strengths show a similar qualitative and quantitative behavior. As one can see, $g(\varphi)$ varies around 0.075 GHz, over the interval $\varphi/2\pi \in [0, 0.5]$, while $\bar{g}(\varphi)$ spans over a range of 0.08 GHz.

Figures 8(a) and 8(b) show the evolution of the effective interaction strength as a function of time t. In Fig. 8(a) we show the effective interaction strength $g(\varphi(t))$ [see Eqs. (29) and (33)] for architecture I. Here we use the same parameters as in Fig. 2(a) to model the control pulse $\varphi(t)$ and the energies listed in Table I, row $i = 2$, to obtain g. In this case we observe fast oscillating variations of g at the order of 1 MHz. Similarly, in Fig. 8(b) we show the effective interaction strength $\bar{g}(\varphi(t))$ [see Eqs. (30) and (33)] for architecture II. Here we use the same control pulse parameters as in Fig. 2(b) and the energies listed in Table II, row $i = 1$. As one can see, in this case we find that if the pulse has reached its plateau, the effective interaction strength has been reduced by about 31 MHz.

Since architecture I is usually operated around a fixed flux offset φ_0, i.e., we only use small pulse amplitudes δ, we would expect that small variations of the effective interaction do not matter too much. The same reasoning would suggest that, in the case of architecture II, the time dependence of $\bar{g}(\varphi)$ is much more relevant since here we vary the external flux over a much larger interval. Furthermore, the unimodal pulse lowers the effective interaction strength temporarily, for about 80% of the total gate duration, and it does not oscillate. However, in the following section we show that this reasoning is not sound. We find that the time-dependent effective interaction strength affects architecture I much more than architecture II. We show this by performing all simulations twice; i.e., we simulate the systems with and without a time-dependent interaction strength.

In Appendix D, we study transitions between states of the circuit Hamiltonian models which can be used to implement iSWAP and CZ gates on different circuit architectures [see circuit Hamiltonians in Eqs. (7) and (8)]. In case of architecture I we applied a harmonic control pulse of the form of Eq. (33) to the tunable coupler. On architecture II we activated transitions between different states by means of a unimodal pulse; i.e., in Eq. (33) we set $\omega^D = 0$. Here we create avoided crossings between different energy levels. In Secs. III C 1 and III C 2 we repeat this analysis with the effective model Hamiltonians in Eqs. (31) and (32) and compare the results with the ones for the circuit Hamiltonian models which can be found in Table VI. A summary of all results for the effective models can be found in Table VII.

1. Architecture I

We consider the model Hamiltonian in Eq. (31). The simulation parameters are listed in Tables I and III. Note that we need the capacitive and Josephson energies if we model the time-dependent effective interaction strength with Eq. (29). We first discuss the two different iSWAP transitions [see Figs. 9(a) and 9(b)] and then the CZ transitions [see Figs. 9(c) and 9(d)]. Afterwards, we further investigate the transitioning from a model with a static effective interaction strength g to a model with a time-dependent effective interaction strength $g(t)$ [see Fig. 10 and Figs. 11(a) and 11(b)].

Figure 9(a) shows the probabilities $p^{(0,0,1)}(t)$ and $p^{(0,1,0)}(t)$ as functions of time t. We use a static effective interaction strength g to model the system; i.e., we use the effective interaction strength which is determined by the flux offset $\varphi_0/2\pi = 0.15$. We find a resonance frequency or optimal drive frequency of $\omega^D = 1.088$ GHz. This frequency deviates only 2 MHz from the one we found for the corresponding

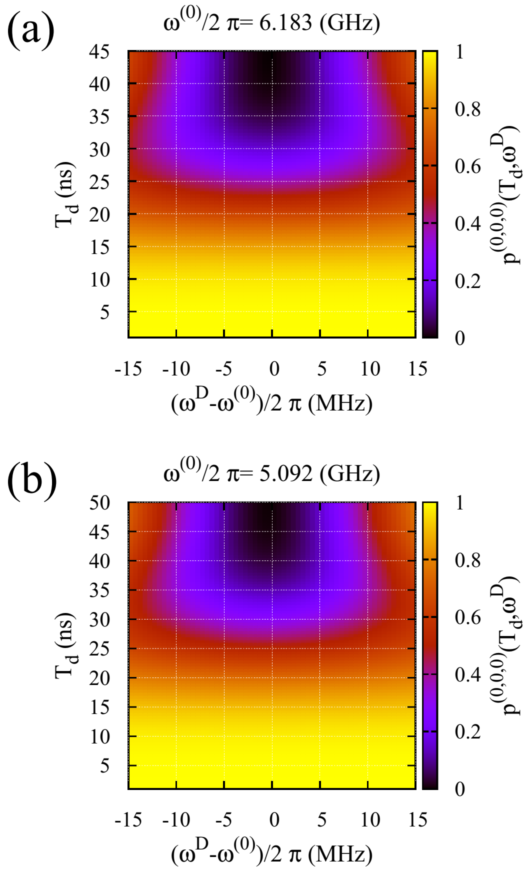

FIG. 6. (a) Chevron pattern for a pulse of the form of Eq. (33) with the drive frequency $\omega^D = 6.183$ GHz and the amplitude $\delta/2\pi = 0.045$. (b) Chevron pattern for a pulse of the form of Eq. (33) with the drive frequency $\omega^D = 5.092$ GHz and the amplitude $\delta/2\pi = 0.085$. We use the same rise and fall time $T_{\mathrm{r/f}} = T_{\mathrm{d}}/2$ for both cases. These patterns show how the circuit Hamiltonian in Eq. (7) (with the parameters listed in Table I) reacts to two different pulses, characterized by the different pulse parameters. The color bar shows the probability $p^{(0,0,0)}$ as a function of the pulse duration time T_{d}. The chevron patterns are used to calibrate control pulses, which are then used to obtain the results in Table VI.

circuit Hamiltonian model (see Table VI). The drive amplitude, which is $\delta/2\pi = 0.075$, is the same amplitude we use in Table VI. However, with these pulse parameters we find a gate duration of 139.6 ns. This means we can implement this gate around 70 ns faster than in the case of the circuit Hamiltonian in Eq. (7) (see Table VI). This is a rather strong difference.

Figure 9(b) shows the probabilities $p^{(0,0,1)}(t)$ and $p^{(0,1,0)}(t)$ as functions of time t. We use a time-dependent effective interaction strength to model the dynamics of the system.

Note that the effective interaction strengths $g(\varphi)$ for an external flux of $\varphi/2\pi = 0.075$ and $\varphi/2\pi = 0.15$ deviate from one another by roughly 3 MHz. Apart from the effective interaction strength, we only adjusted the drive frequency slightly. Here we find an optimal drive frequency of $\omega^D = 1.089$ GHz. As one can see, the gate duration in this case is 205.4 ns. Therefore, we find that the deviations between the gate durations, for both models in Eqs. (7) and (31), decrease to

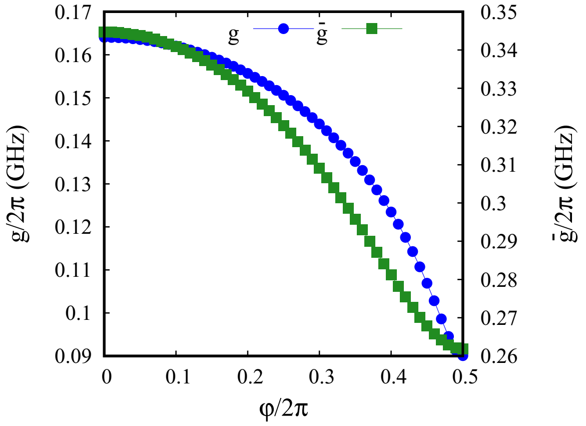

FIG. 7. Effective interaction strengths g [see Eq. (29)] in blue on the left y axis and $\bar{g}$ [see Eq. (30)] in green on the right y axis as functions of the external flux φ. We use the energies listed in Table I ($i = 2$) to obtain g. Similarly, for $\bar{g}$ we use the parameters listed in Table II ($i = 1$).

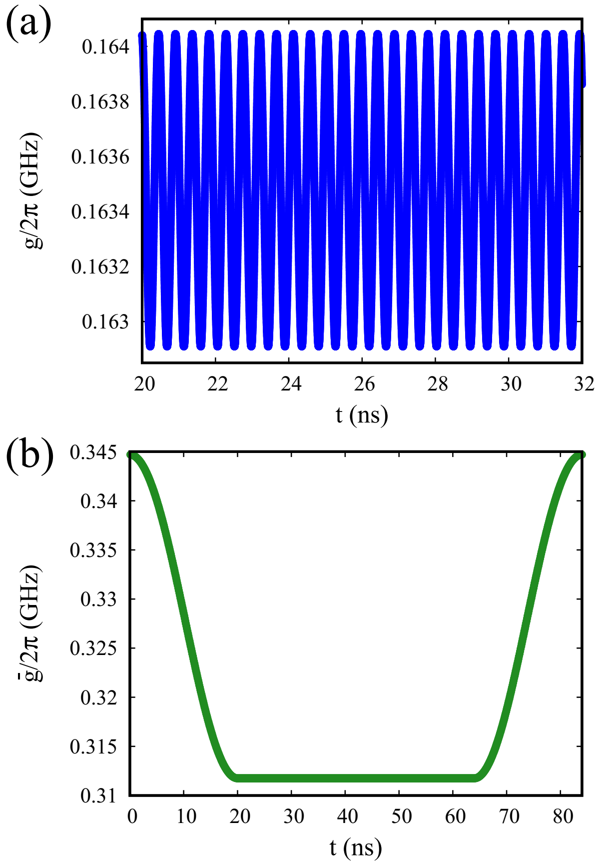

FIG. 8. Effective interaction strength as a function of time for two different flux control pulses. (a) Effective interaction strength $g(\varphi(t))$ [see Eqs. (29) and (33)] for architecture I. We use the energies listed in Table I ($i = 2$) to obtain g and the same control pulse parameters as in Fig. 2(a). These control pulse parameters are also listed in Table VII (row 6). (b) Effective interaction strength $\bar{g}(\varphi(t))$ [see Eqs. (30) and (33)] for architecture II. We use the energies listed Table II ($i = 1$) to obtain $\bar{g}$ and the same control pulse parameters as in Fig. 2(b). These control pulse parameters are also listed in Table VII (row 9).

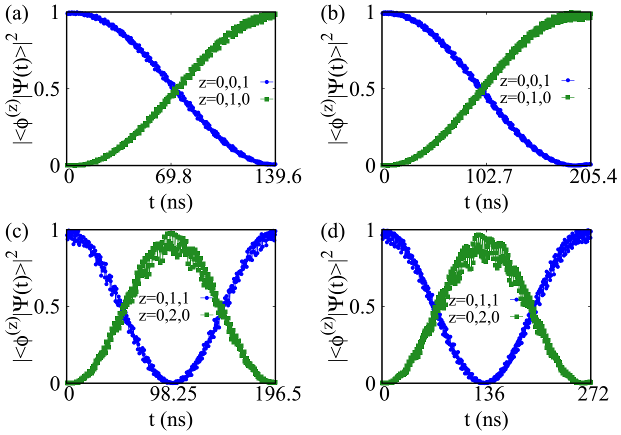

FIG. 9. Probabilities $p^{(z)}(t)$ as functions of time for (a)-(b) $z = (0, 0, 1)$ and $z = (0, 1, 0)$ and (c)-(d) $z = (0, 1, 1)$ and $z = (0, 2, 0)$. In panels (a) and (c) we model the system without a time-dependent effective interaction strength [see Eq. (29)]. In panels (b) and (d) we include the time dependence. In all cases we use the Hamiltonian in Eq. (31), the parameters listed in Tables I and III, and a pulse of the form of Eq. (33) to obtain the results. The pulse parameters are discussed in the main text. The $z = (0, 1, 1) \rightarrow z = (0, 2, 0)$ transitions are usually used to implement CZ operations and the $z = (0, 0, 1) \rightarrow z = (0, 1, 0)$ transitions are often used to realize iSWAP operations (see Refs. [3,13]). Interestingly, we observe a large shift in the pulse duration T_d if we model the system with a time-dependent effective interaction strength [see Fig. 8(a)].

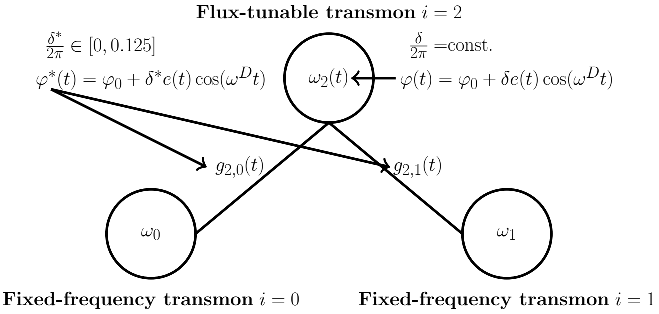

FIG. 10. Functional sketch of the control pulses [see Eq. (33)] we use to determine the results in Figs. 11(a) and 11(b). We use the Hamiltonian given by Eq. (31) and the device parameters listed in Table I to model the dynamics of a system of type architecture I. The intention is to investigate the transition from a model with a static effective interaction strength $g_{j,i}(t)$ given by Eq. (29) with $\delta^*/2\pi = 0$ to a model where the effective interaction strength oscillates with $\delta^*/2\pi \in (0, 0.125]$ [see also Fig. 8(a)]. Therefore, we keep the pulse amplitude δ for the tunable coupler frequency given by Eq. (20) constant. We use $\delta/2\pi = 0.075$ in Fig. 11(a) to model the two-qubit iSWAP transitions and $\delta/2\pi = 0.085$ in Fig. 11(b) to model the two-qubit CZ transitions. Note that these are the same pulse amplitudes we use in Figs. 9(a) and 9(b) and Figs. 9(c) and 9(d), respectively. Furthermore, if $\delta^* = 0$ we simulate the scenarios we show in Figs. 9(a) and 9(c) and if $\delta^* = \delta$ we simulate the scenarios we show in Figs. 9(b) and 9(d). However, in Figs. 11(a) and 11(b) the pulse duration T_d is set to 300 ns for all cases.

4 ns if we model the system with a time-dependent interaction strength.

Figures 9(c) and 9(d) show the same scenarios for the CZ operation; i.e., we display the time evolution of $p^{(1,1,1)}(t)$ and $p^{(0,2,0)}(t)$ for two different models. In Fig. 9(c) we model the system with a time-independent effective interaction strength and in Fig. 9(d) we include the time dependence. In both cases we find the optimal drive frequency $\omega^D = 0.807$ GHz. If we compare this drive frequency with the one we obtained for the circuit Hamiltonian (see Table VI), we see that there is a shift of 2 MHz. Additionally, both control pulses are calibrated with an amplitude of $\delta/2\pi = 0.085$.

We observe that if we model the system with a time-independent effective interaction strength, we find a gate duration of 196.5 ns. Including the time dependence leads to a gate duration of 272 ns. A comparison between these results and the ones given in Appendix D leads to a deviation of around 25 ns if we include the time-dependent effective interaction strength.

In order to better understand the behavior of the transitioning from a model with a static effective interaction strength to a model with a time-dependent effective interaction strength, we performed more simulations. The results are displayed in Figs. 11(a) and 11(b). Additionally, in Fig. 10 we show a functional sketch of the control pulses we use to obtain the results presented in Figs. 11(a) and 11(b).

Figure 10 shows that we use the control pulse in Eq. (33) to model the tunable coupler frequency given by Eq. (20) with a pulse amplitude $\delta/2\pi =$ const and the effective interacting strength given by Eq. (29) with pulse amplitudes $\delta^*/2\pi \in [0, 0.125]$. All the remaining pulse parameters are the same for both pulses. We use $\delta/2\pi = 0.075$ in Fig. 11(a) for the two-qubit gate iSWAP transitions $z = (0, 0, 1) \rightarrow z = (0, 1, 0)$ and $\delta/2\pi = 0.085$ in Fig. 11(b) for the two-qubit gate CZ transitions $z = (0, 1, 1) \rightarrow z = (0, 2, 0)$. If we use $\delta^* = 0$ to model the static effective interaction strength, we model the scenarios we presented in Figs. 9(a) and 9(c). Similarly, if we use $\delta^* = \delta$, we model the scenario we presented in Figs. 9(b) and 9(d). The values in between $\delta^* \in (0, \delta)$ show the transition from one case to the other. Additionally, we added some more amplitudes $\delta^* \in (\delta, 2\pi 0.125]$ to have some additional data which might shine some light on the effect. Note that we use the pulse duration $T_\mathrm{d} = 300$ ns and the rise and fall time $T_{\mathrm{r/f}} = 13$ ns for all simulations.

Figures 11(a) and 11(b) show the probabilities $p^{(z)}(t)$ for $z = (0, 0, 1)$ and $z = (0, 1, 1)$, respectively, as functions of time t for different pulse amplitudes δ^* as explained above (see Fig. 10). We use the Hamiltonian given by Eq. (31) and the parameters listed in Table I to model the dynamics of a system of type architecture I. The control pulses and all pulse parameters except the drive frequency ω^D are discussed in the preceding paragraph.

In Fig. 11(a) we model the iSWAP transitions $z = (0, 0, 1) \rightarrow z = (0, 1, 0)$. Here we use $\omega^D/2\pi = 1.088$ GHz (blue lines and open markers) and $\omega^D/2\pi = 1.089$ GHz (green lines and solid markers) to model the dynamics of $p^{(0,0,1)}(t)$. Note that the drive frequency which leads to full population exchange between the two states involved only shifts by 1 MHz over the range $\delta^*/2\pi \in [0, 0.125]$. As one

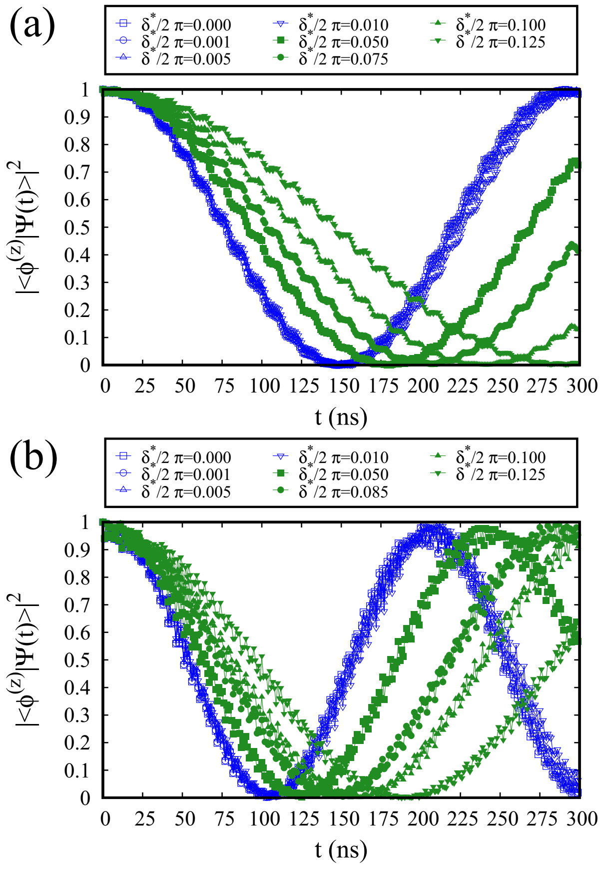

FIG. 11. Probabilities $p^{(z)}(t)$ as functions of time t for (a) $z = (0, 0, 1)$ and (b) $z = (0, 1, 1)$. In (a) we model transitions which might be used to implement iSWAP gates. Similarly, in (b) we model transitions which might be used to implement CZ gates. Here we use the effective Hamiltonian given by Eq. (31), the device parameters listed in Table I, and the pulse in Eq. (33) to obtain the results. The system is modeled with a time-dependent interaction strength $g(t)$ given by Eq. (29). Panels (a) and (b) show the route from the model where we use a static interaction strength, i.e., with pulse amplitude $\delta^* = 0$, to the model where the interaction strength is dynamic, i.e., with pulse amplitude $\delta^* \neq 0$. Here δ^* denotes the amplitude we use to model the time-dependent $g(t)$ given by Eq. (29) [see also Fig. 8(a)]. The procedure is graphically illustrated in Fig. 10. In order to better understand how a time-dependent $g(t)$ affects the dynamics of the system, we turn on the dynamic interaction strength $\delta^*/2\pi \in [0, 0.125]$ while keeping the amplitude δ for the tunable frequency given by Eq. (20) fixed. We use (a) $\delta/2\pi = 0.075$ to model the iSWAP transition and (b) $\delta/2\pi = 0.085$ to model the CZ transition. Note that these are the same amplitudes δ we use to obtain the results in Fig. 9. In this scenario, we need to slightly adjust the drive frequencies ω^D as we increase δ^*. We use $\omega^D/2\pi = 1.088$ GHz (blue lines and open markers) and $\omega^D/2\pi = 1.089$ GHz (green lines and solid markers) to model the iSWAP transitions in (a). Similarly, we use $\omega^D/2\pi = 0.807$ GHz (blue lines and open markers) and $\omega^D 2\pi = 0.808$ GHz (green lines and solid markers) to model the CZ transitions in (b). All results are obtained with the rise and fall time $T_{\mathrm{r/f}} = 13$ ns and the gate duration $T_{\mathrm{d}} = 300$ ns.

can see, at first for $\delta^*/2\pi \in [0, 0.010]$ the qualitative and quantitative behavior of the overall transition $z = (0, 0, 1) \rightarrow z = (0, 1, 0)$ is barely affected by the time-dependent effective interaction strength. Then for $\delta^*/2\pi \in [0.050, 0.125]$ every increase in the pulse amplitude leads to a shift of the first minimum of $p^{(0,0,1)}(t)$ of more than 25 ns.

In Fig. 11(b) we use $\omega^D/2\pi = 0.807$ GHz (blue lines and open markers) and $\omega^D/2\pi = 0.808$ GHz (green lines and solid markers) to model the dynamics of $p^{(z)}(t)$. Here we find a similar qualitative behavior as in Fig. 11(a). At first, the overall behavior of the transition $z = (0, 1, 1) \rightarrow z = (0, 2, 0)$ is not much affected by $g(t)$. Then we can observe how the first minimum of $p^{(0,1,1)}(t)$ moves roughly in steps of 25 ns to the right of the x axis.

The results presented in Figs. 9(a)–9(d) and Figs. 11(a) and 11(b) lead to the question of why the oscillations of the effective interaction strength $g(t)$ are so relevant. However, even after performing more simulations, we were not able to find a conclusive theoretical explanation for this effect. Here we simulated the time evolution of the spectrum and the relevant probabilities while turning on and off various time dependencies in the model. We leave this problem for future research.

Additionally, we also simulated the effective model given by Eq. (31) with an additional nonadiabatic drive term given by Eq. (21), for the flux-tunable coupler. Here we find (data not shown) that the iSWAP $z = (0, 0, 1) \rightarrow z = (0, 1, 0)$ and CZ $z = (0, 1, 1) \rightarrow z = (0, 2, 0)$ transitions are barely affected by the nonadiabatic drive term. Note that we tested this only for the pulse parameters listed in Table VII in rows 7–10.

The remaining deviations between the effective and circuit model might be attributed to additional approximations made. For instance, we model the interaction between the different subsystems with an operator which is the result of a perturbative analysis (see Ref. [9]). Second, Ref. [23] shows that such approximations can lead to deviations which increase with time; in this case a free time evolution was considered.

In general, we find that if we consider short time scales of around 250 ns, both Hamiltonians in Eq. (7) and Eq. (31) predict similar outcomes for only marginally different control pulses if we model the system with a time-dependent interaction strength.

2. Architecture II

In the following, we compare the results of the second circuit Hamiltonian in Eq. (8) with the ones we obtain for the Hamiltonian given by Eq. (32). Here we use the parameters listed in Tables II and IV to obtain the results. Note that we need the parameters in Table II if we model the system with a time-dependent interaction strength and an adjusted spectrum [see Eqs. (B2) and (B3)]. Furthermore, we use a pulse of the form of Eq. (33) with $\omega^{\mathrm{D}} = 0$ and $T_{\mathrm{r/f}} = 20$ ns in all cases. As before, we first discuss the iSWAP gate [see Figs. 12(a) and 12(b)] and then the CZ gate [see Figs. 12(c) and 12(d)].

Figure 12(a) shows the probabilities $p^{(0,0,1)}(t)$ and $p^{(0,1,0)}(t)$ as functions of time t. We use a time-independent effective interaction strength to model the dynamics of the system. We find the optimal drive amplitude $\delta/2\pi = 0.297$ and a gate duration of $T_{\mathrm{d}} = 84$ ns. Consequently, we observe a 16-ns discrepancy if we compare these results with the one we obtained for the circuit Hamiltonian model (see Table VI). Furthermore, the pulse amplitude has shifted. This can be explained by the fact that the flux-tunable frequency

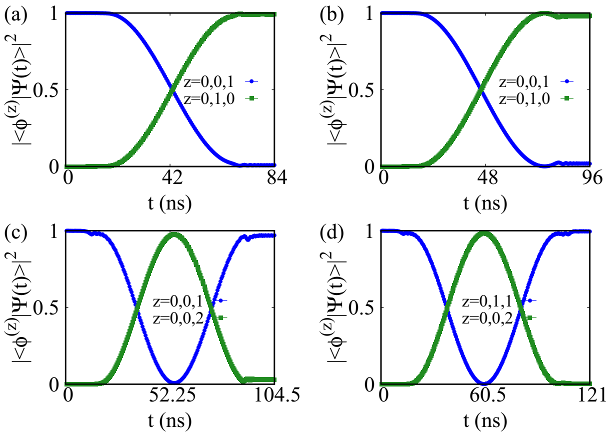

FIG. 12. Probabilities $p^{(z)}(t)$ as functions of time for (a)-(b) $z = (0, 0, 1)$ and $z = (0, 1, 0)$ and (c)-(d) $z = (0, 1, 1)$ and $z = (0, 0, 2)$. In panels (a) and (c) we model the system without a time-dependent effective interaction strength [see Eq. (30)]. In panels (b) and (d) we include the time dependence. In all cases we use the Hamiltonian in Eq. (32), the parameters listed in Tables II and IV, and a pulse of the form of Eq. (33) to obtain the results. The pulse parameters are discussed in the main text. The $z = (0, 1, 1) \rightarrow z = (0, 2, 0)$ transitions are usually used to implement CZ operations and the $z = (0, 0, 1) \rightarrow z = (0, 1, 0)$ transitions are often used to realize iSWAP operations. We observe a modest shift in the pulse duration $T_{\rm d}$ if we model the system with a time-dependent effective interaction strength [see Fig. 8(b)].

of the effective model $\omega(\varphi)$ as well as the corresponding anharmonicity α start to deviate from the numerically exact spectrum for large external fluxes φ [see Appendix B and Figs. 13(a) and 13(b)].

We can correct the spectrum by using more accurate expressions [see Eqs. (B2) and (B3)] for the qubit frequency and the anharmonicity. Figure 12(b) shows the probabilities $p^{(0,0,1)}(t)$ and $p^{(0,1,0)}(t)$ as functions of time t. Here we model the system with a time-dependent effective interaction strength $\bar{g}(t)$ [see Eq. (30)]. Furthermore, we also adjust the spectrum. We find the optimal pulse amplitude $\delta/2\pi = 0.289$. This is the same amplitude we determined for the circuit Hamiltonian in Eq. (8) (see Table VI). We find a gate duration of 96 ns. Therefore, the discrepancies between the different gate duration times have decreased to 4 ns. Note that this is the same deviation we found for the other system, when we modeled the iSWAP operation.

We also simulated the case (data not shown) where only the spectrum is adjusted and the effective interaction strength is constant. As before, we compute the tunable qubit frequency and anharmonicity with the series expansions in Eqs. (B2) and (B3). Here we also find an optimal pulse amplitude $\delta/2\pi = 0.289$. Therefore, we conclude that this is purely a consequence of the deviations in the qubit frequency and anharmonicity [see Appendix B and Figs. 13(a) and 13(b)].

Figures 12(c) and 12(d) show the probabilities $p^{(0,1,1)}(t)$ and $p^{(0,0,2)}(t)$ as functions of time t. Here we model the CZ gate with two different model Hamiltonians, i.e., with and without the time-independent effective interaction strength and an adjusted spectrum. Figures 12(c) and 12(d) show the same characteristics as Figs. 12(a) and 12(b). We find that if we do not use an adjusted spectrum, the optimal control pulse amplitude δ requires adjustment. Furthermore, if we assume that the effective interaction strength is constant, we find a gate duration which is about 20 ns shorter. If we adjust the spectrum, we find that the shift of the optimal drive amplitude disappears. Similarly, if we include the time-dependent effective interaction strength, we see that the gate duration increases to 121 ns. This means the differences between the effective and the circuit Hamiltonian model decrease to 4 ns. Therefore, we might conclude that the time dependence of the effective interaction strength is not negligible if the aim is to approximate the time evolution of the corresponding circuit Hamiltonian.

Finally, we also simulated the effective model given by Eq. (32) with additional nonadiabatic drive terms given by Eq. (21), for the flux-tunable transmon qubits. Here we find (data not shown) that the iSWAP $z = (0, 0, 1) \rightarrow z = (0, 1, 0)$ and CZ $z = (0, 1, 1) \rightarrow z = (0, 0, 2)$ transitions are barely affected by the nonadiabatic drive terms which we add to the model. Note that we tested this only for the pulse parameters listed in Table VII in rows 11–14.

In summary, we observe that if we adjust the spectrum of the effective model and include the time dependence of the effective interaction strength, the effective Hamiltonian in Eq. (32) and the circuit Hamiltonian in Eq. (8) predict similar outcomes. However, we also found that unless the model is adjusted properly, the outcomes can deviate quite strongly. Note that the deviations are already observable for the rather small time scales considered here, and such deviations typically tend to grow with time.

IV. SUMMARY AND CONCLUSIONS

We have implemented two simulators to solve the TDSE for two different but related generic models of a superconducting quantum processor. The first model is a lumped-element model, i.e., a circuit Hamiltonian. The second model is an approximation of the first one, i.e., an effective model Hamiltonian. Both models aim to describe a set of interacting transmon qubits (fixed frequency and/or flux tunable) and transmission line resonators. The interaction between the different subsystems is always of the dipole-dipole type.

The first simulation code, for the circuit Hamiltonian model, enables us to simulate the model without making any approximations. The second simulation code, for the effective Hamiltonian model, allows us to simulate the system with various approximations being turned on or off. A basic version of the simulation code for the effective model is available at Ref. [24]. This simulation framework provides us with the tools to study the validity of different approximations, which are often made to make analytical calculations feasible.

For our study we consider three different systems. The first system is a single flux-tunable transmon. The second system, architecture I, consists of two fixed-frequency transmons, coupled to a flux-tunable transmon. The flux-tunable transmon works as a coupler [see Fig. 1(a)]. The third system, architecture II, is made up of two flux-tunable transmons, coupled to a transmission line resonator. Here the resonator functions only as a coupler element [see Fig. 1(b)].

We found that the effective model Hamiltonian given by Eq. (18) allows us to approximate the dynamic behavior of the circuit Hamiltonian in Eq. (2) quite well. However, for some transition scenarios some deviations still remain [see Figs. 5(d) and 5(h)]. Furthermore, as can be expected, the adiabatic effective Hamiltonian in Eq. (25) cannot describe any dynamic transitioning behavior. The results are discussed in Sec. III A.

In addition, it seems that if we use the adiabatic effective Hamiltonian in Eq. (25) to model flux-tunable transmons in multiqubit systems [see the effective model Hamiltonian given by Eq. (31)], we suppress additional resonant transitions. A summary of these results is provided in Table VII (see the rightmost column). However, we can recover these resonant transitions by adding the nonadiabatic drive term in Eq. (21) to every flux-tunable transmon in the effective model Hamiltonian. The results are discussed in Sec. III B. Once larger superconducting processors are built, with more than a few transmon qubits, we face the problem of spectral crowding. However, if we base our analysis of this problem only on the transition frequencies which are relevant for the effective model, we might overlook frequencies which are crucial for this issue.

Our analysis shows that assuming the effective interaction strength to be time independent can affect the gate durations of some two-qubit gates quite strongly. Here we consider the difference between two effective models, with and without a time-dependent interaction strength and the difference with respect to the circuit Hamiltonian model. A summary of these results can be found in Table VII (see the second-to-last column). For example, if we model two-qubit CZ gate interactions in architecture I [see Fig. 1(a)], with and without a time-dependent interaction strength and the effective Hamiltonian given by Eq. (31), we find that the gate duration deviates up to about 75 ns. The deviations with respect to the circuit Hamiltonian model for the same transitions are about 100 ns if we do not include the time dependence into the effective model. These deviations seem too large to be neglected. The time-dependent effective interaction strength affects the gate durations of architecture II [see Fig. 1(b)] to a lesser extent. Additionally, we found that for the pulses we model in this work, the nonadiabatic drive term in Eq. (21) barely affects the two-qubit gate transitions in architectures I and II. The results are discussed in Sec. III C.

The focus of our analysis has been put on the dynamics of the very basic state-transition mechanism. For future work, it might be interesting to see whether or not the different models generate different error signatures, once complete quantum circuits are simulated (see Ref. [10]). It seems plausible that these errors are very sensitive to changes to the model. The challenge here is to make a fair comparison between two different models that are parametrized in terms of the pulse parameters.

ACKNOWLEDGMENTS

The authors gratefully acknowledge the Gauss Centre for Supercomputing e.V. [25] for funding this project by providing computing time on the GCS Supercomputer JUWELS [26] at Jülich Supercomputing Centre (JSC). H.L. acknowledges support from the project OpenSuperQ (820363) of the EU Quantum Flagship. D.W.'s work was partially supported by the Q(AI)^2 project. D.W. and M.W. acknowledge support from the project Jülich UNified Infrastructure for Quantum computing (JUNIQ) that has received funding from the German Federal Ministry of Education and Research (BMBF) and the Ministry of Culture and Science of the State of North Rhine-Westphalia.

APPENDIX A: DERIVATION OF THE EFFECTIVE HAMILTONIAN FOR A FLUX-TUNABLE TRANSMON BY MEANS OF A COSINE EXPANSION

The goal of the main text was to present a comparison between the descriptions of the full circuit Hamiltonian in Eq. (2) and the effective Hamiltonian given by Eq. (25). In this Appendix, we outline the steps that are often implicitly made to derive the effective Hamiltonian. Note that throughout this work we use $\hbar = 1$.

We derive the effective Hamiltonian given by Eq. (25) in a stepwise manner. We start from the circuit Hamiltonian

$$\hat{H}_{\text{Tun}} = E_C \hat{n}^2 - E_{J,\text{eff}}(t)\cos(\hat{\varphi} - \varphi_{\text{eff}}(t)), \tag{A1}$$

given by Eq. (13) in the main text, and perform an expansion of the cosine to second order. The corresponding second-order expansion reads

$$\hat{H} = E_C \hat{n}^2 + \frac{E_{J,\text{eff}}(t)}{2}(\hat{\varphi} - \varphi_{\text{eff}}(t))^2, \tag{A2}$$

where we neglect the $-E_{J,\text{eff}}(t)$ term which only contributes a nonmeasurable phase to the dynamics of the system. We obtain the instantaneous eigenstates in φ space for this Hamiltonian,

$$\psi^{(m)}(x(t)) = \frac{1}{\sqrt{2^m m!}}\left(\frac{\xi(t)}{\pi}\right)^{\frac{1}{4}} e^{-\frac{x^2(t)}{2}} \mathcal{H}_m(x(t)), \tag{A3}$$

where $\xi(t) = (E_{J,\text{eff}}(t)/2E_C)^{1/2}$, $x(t) = \sqrt{\xi(t)}(\varphi - \varphi_{\text{eff}}(t))$, and $\mathcal{H}_m$ denotes the Hermite polynomial of order m. The corresponding eigenvalues

$$E^{(m)}(t) = \omega(t)m + 1/2, \tag{A4}$$

where $\omega(t) = \sqrt{2E_C E_{J,\text{eff}}(t)}$, can be determined analytically.

We intend to model the system in the time-dependent basis

$$\mathcal{B}(t) = \{|\psi^{(m)}(t)\rangle\}_{m\in\mathbb{N}}, \tag{A5}$$

such that the transformed state vector reads

$$|\Psi^*(t)\rangle = \hat{\mathcal{W}}(t)\,|\Psi(t)\rangle\,, \tag{A6}$$

where $\hat{\mathcal{W}}(t)$ denotes the unitary transformation which maps the basis states $\mathcal{B}(0)$ to the basis states $\mathcal{B}(t)$. This requires that we transform the Hamiltonian operator

$$\hat{H}^*(t) = \hat{\mathcal{W}}(t)\hat{H}(t)\hat{\mathcal{W}}^\dagger(t) - i\hat{\mathcal{W}}(t)\partial_t\hat{\mathcal{W}}^\dagger(t), \tag{A7}$$

such that TDSE for the state $|\Psi^*(t)\rangle$ retains its original form (see Refs. [20,27]).

The drive term

$$\hat{\mathcal{D}}(t) = -i\hat{\mathcal{W}}(t)\partial_t\hat{\mathcal{W}}^\dagger(t) \tag{A8}$$

in Eq. (A7) can be expressed as

$$\hat{\mathcal{D}}(t) = -i\sqrt{\frac{\xi(t)}{2}}\dot{\varphi}_{\text{eff}}(t)(\hat{b}^{\dagger} - \hat{b}) + \frac{i}{4}\frac{\dot{\xi}(t)}{\xi(t)}(\hat{b}^{\dagger}\hat{b}^{\dagger} - \hat{b}\hat{b}), \quad \text{(A9)}$$

where we assume that $\xi(t) \neq 0$ for all times t. Here we adjusted a derivation which can be found in Sec. 5.1.2 of Ref. [27]. We also find

$$\dot{\varphi}_{\text{eff}}(t) = \dot{\varphi}(t)\frac{d}{2\big(\cos\big(\frac{\varphi(t)}{2}\big)^2 + d^2\sin\big(\frac{\varphi(t)}{2}\big)^2\big)} \quad \text{(A10)}$$

and

$$\frac{\dot{\xi}(t)}{\xi(t)} = \dot{\varphi}(t)\frac{(d^2-1)\sin(\varphi(t))}{8\big(\cos\big(\frac{\varphi(t)}{2}\big)^2 + d^2\sin\big(\frac{\varphi(t)}{2}\big)^2\big)}, \quad \text{(A11)}$$

so that the first (second) drive term in Eq. (A9) disappears if $d = 0$ $(d = 1)$.

The Hamiltonian in the time-dependent harmonic basis reads

$$\begin{aligned}\hat{H}_1^{*} &= \omega(t)\hat{b}^{\dagger}\hat{b}\\ &\quad + -i\sqrt{\frac{\xi(t)}{2}}\dot{\varphi}_{\text{eff}}(t)(\hat{b}^{\dagger} - \hat{b})\\ &\quad + \frac{i}{4}\frac{\dot{\xi}(t)}{\xi(t)}(\hat{b}^{\dagger}\hat{b}^{\dagger} - \hat{b}\hat{b}).\end{aligned} \quad \text{(A12)}$$

Here we made use of the definitions

$$\hat{n} = -\sqrt{\frac{\xi(t)}{2}}(\hat{b}^{\dagger} + \hat{b}) \quad \text{(A13)}$$

and

$$(\hat{\varphi} - \varphi_{\text{eff}}(t)\hat{I}) = \frac{-i}{\sqrt{2\xi(t)}}(\hat{b}^{\dagger} - \hat{b}), \quad \text{(A14)}$$

for the charge and the shifted flux operator, respectively.

If one models the system with two basis states only, one can express the Hamiltonian in terms of the Pauli $\hat{\sigma}^{(z)}$ and $\hat{\sigma}^{(y)}$ operators. The result reads

$$\hat{H}_{1,I}^{*} = -\frac{\omega(t)}{2}\hat{\sigma}^{(z)} - \sqrt{\frac{\xi(t)}{2}}\dot{\varphi}_{\text{eff}}(t)\hat{\sigma}^{(y)}. \quad \text{(A15)}$$

The term $-(\omega(t)/2)\hat{\sigma}^{(z)}$ is sometimes used to model flux-tunable transmons as two-level systems (see Refs. [6,7,18]). Obviously, in such a case, one neglects the contribution of the higher-order terms in the cosine expansion. Furthermore, one neglects all contributions of the drive term $\hat{\mathcal{D}}(t)$ which originated from the fact that we use a time-dependent basis to describe the dynamics.

We now expand the cosine to the quartic order and neglect all terms which only contribute a nonmeasurable phase. The corresponding effective Hamiltonian reads

$$\begin{aligned}\hat{H}_2 &= E_C\hat{n}^2 + \frac{E_{J,\text{eff}}(t)}{2}(\hat{\varphi} - \varphi_{\text{eff}}(t))^2\\ &\quad - \frac{E_{J,\text{eff}}(t)}{24}(\hat{\varphi} - \varphi_{\text{eff}}(t))^4.\end{aligned} \quad \text{(A16)}$$

If we model the system in the basis $\mathcal{B}(t)$, we find the Hamiltonian

$$\hat{H}_2^{*} = \omega(t)\hat{b}^{\dagger}\hat{b} - \frac{E_C}{48}(\hat{b}^{\dagger} - \hat{b})^4 + \hat{\mathcal{D}}(t). \quad \text{(A17)}$$

One can split the operator

$$(\hat{b}^{\dagger} - \hat{b})^4 = \hat{D} + \hat{V} \quad \text{(A18)}$$

into a diagonal $\hat{D}$ and an off-diagonal part $\hat{V}$. We make use of this decomposition and define another effective Hamiltonian,

$$\hat{H}_{2,I}^{*} = \omega'(t)\hat{b}^{\dagger}\hat{b} + \frac{\alpha}{2}\hat{b}^{\dagger}\hat{b}(\hat{b}^{\dagger}\hat{b} - \hat{I}) + \hat{\mathcal{D}}(t), \quad \text{(A19)}$$

where we only keep the diagonal contributions $\hat{D}$ of the operator given by Eq. (A18). Here $\omega'(t) = \omega(t) + \alpha$. Additionally, we define the effective Hamiltonian

$$\hat{H}_{2,II}^{*} = \omega'(t)\hat{b}^{\dagger}\hat{b} + \frac{\alpha}{2}\hat{b}^{\dagger}\hat{b}(\hat{b}^{\dagger}\hat{b} - \hat{I}), \quad \text{(A20)}$$

where we only take into account the diagonal part $\hat{D}$ but neglect the operator $\hat{V}$ and the drive term $\hat{\mathcal{D}}(t)$. We emphasize that this Hamiltonian is often used (see Refs. [3,6–8]) to describe flux-tunable transmons and the subject of the main text.

It should be obvious that neglecting the drive term $\hat{\mathcal{D}}(t)$ in Hamiltonian Eq. (A20) prevents us from modeling transitions between the different basis states in $\mathcal{B}(t)$; i.e., dropping the drive term makes the Hamiltonian in Eq. (A20) diagonal in the basis $\mathcal{B}(t)$. Note that here we consider the route from the model given by Eq. (A17) to the model given by Eq. (A20). The drive term in Eq. (A19) still allows us to model transitions between the different basis states of the system.

In principle, if one defines an effective Hamiltonian $\hat{H}_{\text{E}}(t)$ by dropping one or more terms in a given model Hamiltonian $\hat{H}_{\text{M}}(t)$, one has to consider how the time-evolution operators

$$\hat{\mathcal{U}}_{\text{E}}(t, t_0) = \mathcal{T}\exp\left(-i\int_{t_0}^{t}\hat{H}_{\text{E}}(t')dt'\right) \quad \text{(A21)}$$

and

$$\hat{\mathcal{U}}_{\text{M}}(t, t_0) = \mathcal{T}\exp\left(-i\int_{t_0}^{t}\hat{H}_{\text{M}}(t')dt'\right) \quad \text{(A22)}$$

deviate from one another, and not only the Hamiltonians themselves. Consequently, one has to consider an appropriate operator norm. A general discussion of this subject, with explicit examples, is provided by Ref. [28].

This makes approximating time-dependent Hamiltonians a rather complex subject. For example, dropping the drive term $\hat{\mathcal{D}}(t)$ only constitutes to a kind of adiabatic approximation for a single flux-tunable transmon (see Ref. [20]). However, the adiabatic approximation is formulated in terms of the instantaneous eigenstates of a system. Therefore, once we describe a collection of interacting transmons, we have to reconsider how the corresponding time-evolution operators for the effective model $\hat{\mathcal{U}}_{\text{E}}$ and the original model $\hat{\mathcal{U}}_{\text{M}}$ deviate; i.e., in this case we have to reconsider the error which is caused by defining the effective Hamiltonian. Additionally, in general one cannot predict how dropping different terms [see Eqs. (A19) and (A20)] changes the deviations with respect to the original model [see Eq. (A17) or Eq. (A1)]. Therefore, we decided to simulate both models independently, and to compare their predictions as shown in the main text (see Sec. III A).

APPENDIX B: SERIES EXPANSION OF THE QUBIT FREQUENCY AND ANHARMONICITY

In the main text (see Sec. III), we model various single-qubit and two-qubit transitions with effective and circuit Hamiltonian models. If we compare the pulse parameters for some of these transitions (see Sec. III A and Tables VI and VII), we find that some of these are parameters which one can associate with the energy of a flux-tunable transmon deviate. Consequently, these differences might be attributed to the fact that, if we model the energies of flux-tunable transmons with the expression

$$E^{(m)}(\varphi(t)) - E^{(0)}(\varphi) = m\omega(\varphi) + \frac{\alpha(\varphi)}{2}m(m-1), \qquad \text{(B1)}$$

the results are not accurate for some choices of the external fluxes φ. Here $\omega(\varphi)$ denotes the tunable frequency given by Eq. (20) and $\alpha(\varphi) = \text{const}$ is the anharmonicity of the flux-tunable transmon. Note that throughout this work we use $\hbar = 1$. Furthermore, we removed the explicit time dependence $\varphi(t) \to \varphi$ since the spectrum exhibits symmetries with respect to the variable φ [see Hamiltonian Eq. (2)]. In this Appendix, we compare the spectra of the circuit Hamiltonian given by Eq. (2) with the one of the effective flux-tunable transmon given by Eq. (25). Furthermore, it is possible to make use of alternative expressions which allow us to approximate the spectrum with higher precision. Two such expressions were given in Ref. [29]. The corresponding flux-tunable transmon qubit frequency is of the form

$$\tilde{\omega}(\varphi) = \sqrt{2E_C E_{J_{\text{eff}}}(\varphi)} - \frac{E_C}{4}\sum_{n=0}^{24} a_n \xi(\varphi)^n. \qquad \text{(B2)}$$

Similarly, the flux-dependent qubit anharmonicity can be expressed as

$$\tilde{\alpha}(\varphi) = -\frac{E_C}{4}\sum_{n=0}^{24} b_n \xi(\varphi)^n, \qquad \text{(B3)}$$

where a_n and b_n are real coefficients and the function $\xi(\varphi)$ can be expressed as

$$\xi(\varphi) = \sqrt{\frac{E_C}{2E_{J_{\text{eff}}}(\varphi)}}. \qquad \text{(B4)}$$

We emphasize that the parameters a_n and b_n can be of order 10^6 for large n. Furthermore, for some system parameters, we found this to be the case for a system with an asymmetry factor $d = 0$; we find that $\xi(\varphi) \to 1$ if $\varphi/2\pi \to 0.5$. Here the approximation can break down.

In the following, the flux-tunable frequencies $\omega(\varphi)$ and $\tilde{\omega}(\varphi)$ and the anharmonicities $\alpha(\varphi)$ and $\tilde{\alpha}(\varphi)$ are only given by the functions we specify; i.e., we do not include further corrections. Figures 13(a) and 13(b) show the deviations

$$\Delta\big(E^{(m)}(\varphi) - E^{(0)}(\varphi)\big) = \Big|\big(E^{(m)}_{\text{exact.}}(\varphi) - E^{(0)}_{\text{exact.}}(\varphi)\big) - \left(m\omega(\varphi) + \frac{\alpha(\varphi)}{2}m(m-1)\right)\Big|, \qquad \text{(B5)}$$

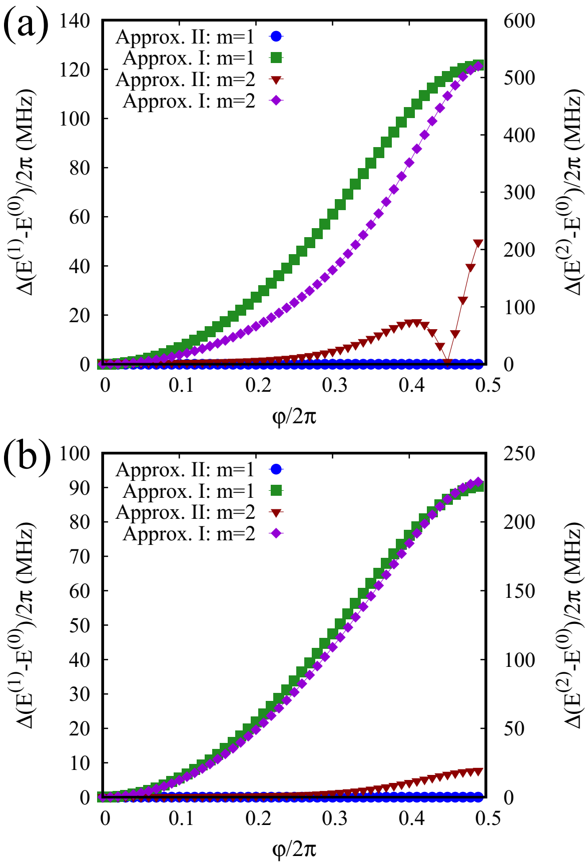

FIG. 13. Deviations between the numerically exact spectrum and two different approximations of this spectrum as a function of the external flux φ for an asymmetry factor (a) $d = 0.33$ and (b) $d = 0.5$. First, we compute the numerically exact spectrum with 50 charge states. Then we use two different sets of expressions for the qubit frequency and anharmonicity to determine the approximated spectrum with Eq. (B1). Approximation I: $\omega(\varphi)$ is given by Eq. (20) and $\alpha(\varphi) = \text{const}$. Approximation II: $\tilde{\omega}(\varphi)$ is given by Eq. (B2) and $\tilde{\alpha}(\varphi)$ is given by Eq. (B3). In the end, we use Eq. (B5) to determine the deviations between the numerically exact energies and the different approximants (see approximations I and II). We use the capacitive and Josephson energies as well as the qubit frequency and anharmonicity listed in Table II, rows (a) $i = 0$ and (b) $i = 1$.

for $m = 1$ (on the left y axis in green and blue) and $m = 2$ (on the right y axis in red and violet) between the numerically exact spectrum of the Hamiltonian in Eq. (2) and two different sets of expressions for the qubit frequency and anharmonicity in Eq. (B5) as a function of the external flux φ. First, we use the parameters listed in Table II, rows $i = 0$ [Fig. 13(a)] and $i = 1$ [Fig. 13(b)], to compute the numerically exact values for two different asymmetry factors $d = 0.33$ [Fig. 13(a)] and $d = 0.5$ [Fig. 13(b)]. Then we compute the approximated spectrum by means of Eq. (B1). Here we consider two different approximations.

Approximation I: We use Eq. (20) for $\omega(\varphi)$, $\alpha(\varphi) = \text{const}$, and Eq. (B1) to compute the energies.

Approximation II: We use the series expansions $\tilde{\omega}(\varphi)$, $\tilde{\alpha}(\varphi)$ [see Eqs. (B2) and (B3), respectively] and Eq. (B1) to do the same. Both Eqs. (B2) and (B3) were taken from Ref. [29].

Note that for $m = 1$ [see Eqs. (B1) and (B5)] the deviations between the different spectra become independent of $\alpha(\varphi)$.

As one can see, approximation I, i.e., the first set of expressions, Eq. (20) and $\alpha(t) = \text{const}$, deviates more from the exact solution than approximation II, i.e., Eqs. (B2) and (B3). In both cases, the deviations grow as the external flux φ approaches the value 0.5. Furthermore, the asymmetry factor d seems to influence how well the spectrum is approximated. If we compare Figs. 13(a) and 13(b), we find that in Fig. 13(b) the deviations can be smaller, e.g., by a factor of 10 [compare the right y axis of Figs. 13(a) and 13(b)].

The deviations in the spectrum can change the behavior of the system once a flux pulse is applied. In particular, if we implement nonadiabatic two-qubit gates (see Refs. [5,30]), the spectrum determines whether or not transitions occur. This becomes even more important if we consider several flux-tunable transmon qubits in one system. Here the errors, in terms of the spectrum, might add up and enhance or suppress different transitions between states. Therefore, an accurate modeling of the spectrum is important.

APPENDIX C: SIMULATION ALGORITHM

In this Appendix, we discuss how we obtain the numerical results presented in Sec. III.

The formal solution of the TDSE (with $\hbar = 1$)

$$i\partial_t \left|\Psi(t)\right\rangle = \hat{H}(t) \left|\Psi(t)\right\rangle , \tag{C1}$$

for an arbitrary time-dependent Hamiltonian $\hat{H}(t)$, reads

$$\hat{\mathcal{U}}(t, t_0) = \mathcal{T} \exp\left(- i \int_{t_0}^{t} \hat{H}(t')dt' \right), \tag{C2}$$

where $\mathcal{T}$ is the time-ordering symbol. Numerical calculations require that this expression is discretized, with steps of length τ. The corresponding time-evolution operator,

$$\hat{U}(t + \tau, t) = \exp\left(- i\tau\hat{H}\left(t + \frac{\tau}{2}\right)\right), \tag{C3}$$

can then be implemented for every time step (using the mid-point rule [31]).

In this work we use the so-called product-formula algorithm (see Refs. [32,33]) to solve the TDSE. This algorithm is explicit, inherently unitary, and unconditionally stable by construction. Here the time-step parameter τ needs to be chosen small enough, with respect to the energy scales and the other relevant time scales of $\hat{H}(t)$, such that the exact mathematical solution of the TDSE is obtained up to some fixed numerical precision. Practically, this means that we decrease τ until it is small enough such that the relevant decimals do not change anymore. This procedure has to be repeated every time we make changes to the system, i.e., if we change the system parameters or the control pulse parameters.

Furthermore, to compute, e.g., the spectrum of a Hamiltonian, we use a standard diagonalization algorithm to obtain the eigenvalues and eigenstates of a Hamiltonian $\hat{H}(t)$.

The simulations of resonant transitions in the effective single flux-tunable transmon model [see Eq. (18)] in Sec. III A require at least four instantaneous basis states. Furthermore, the simulations of nonadiabatic transitions in Sec. III A are performed with 20 instantaneous basis states.

For the simulations of the effective two-qubit models [see Eqs. (31) and (32)] in Secs. III B and III C we use four basis states for all fixed-frequency transmons, flux-tunable transmons, and also for the resonators. The simulation basis here consists of the bare harmonic basis states.

The simulations of the circuit models are performed in the bare transmon basis (for more details see Appendix D). Here we use as many states as necessary; i.e., we increase the number of basis states, N_m, for all transitions we model until the numerical values of the observables converge to some fixed numerical precision. This allows us to obtain an approximation-free, numerical solution of the TDSE for the circuit Hamiltonian.

APPENDIX D: CIRCUIT HAMILTONIAN SIMULATIONS

In this Appendix we discuss the results of the circuit Hamiltonian simulations. A summary of the relevant results can be found in Table VI. We begin with a discussion of the simulation details in Sec. D 1. Then, in Sec. D 2, we discuss the transitions which are suppressed in the effective model (see Sec. III B). In the end, in Sec. D 3, we discuss the transitions which are unsuppressed in the effective model (see Sec. III C).

1. Simulation of circuit Hamiltonians in the transmon basis

If we intend to simulate the circuit Hamiltonians given in Eqs. (2), (7), and (8) without performing any approximations, we can perform the simulations in the transmon bare basis

$$\left|\phi^{(z)}\right\rangle = \bigotimes_{j=0}^{J-1} \left|\phi^{(m_j)}\right\rangle , \tag{D1}$$

where $z = m_0, \ldots, m_{J-1}$ is a placeholder for the different subsystem indices m_j. We form this basis by means of the bare basis states

$$\left|\phi^{(m_j)}\right\rangle \tag{D2}$$

of the corresponding subsystems. These states are the eigenstates of the Hamiltonians given in Eqs. (1), (2), and (4) at time $t = 0$. For simplicity, we call this basis the transmon basis. We need to be able to change the number of basis states, N_m, to allow us to extend the basis up to the point where the relevant decimals of the observables do not change anymore. The numerical error which stems from the discretization of the time domain can be controlled by decreasing the time grid parameter τ up to a point where convergence has been reached. Obviously, both parameters N_m and τ have to be changed together.

We are satisfied with the accuracy if the probabilities

$$p^{(z)}(t) = \left|\left\langle\phi^{(z)}\middle|\Psi(t)\right\rangle\right|^2 \tag{D3}$$

we are interested in agree to the third decimal. Here $\left|\Psi(t)\right\rangle$ denotes the solution of the TDSE. Note that we use at least three basis states for the transmons in the system. If not stated otherwise, transmission line resonators are modeled with four states.

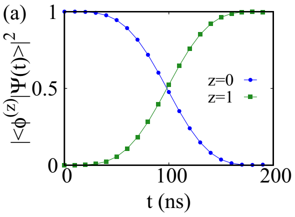

FIG. 14. Probabilities $p^{(0)}(t)$ and $p^{(1)}(t)$ as functions of time t. We use three transmon basis states $N_m = 3$ to model the dynamics of the system, a control pulse of the form of Eq. (33), and a drive frequency ω^D equal to the qubit frequency ω (see Table I, row $i = 2$). The rise and fall time $T_{r/f}$ is set to half the duration time T_d. The system is initialized in the state $|\psi^{(0)}\rangle$. The pulse amplitude $\delta/2\pi$ is set to (a) $\delta/2\pi = 0.001$ and (b) $\delta/2\pi = 0.01$. We can observe that an increase in the pulse amplitude δ by a factor of 10 leads to a decrease of the pulse duration T_d by a factor of 10 (roughly). Note that these transitions cannot be modeled with the effective Hamiltonian in Eq. (25).

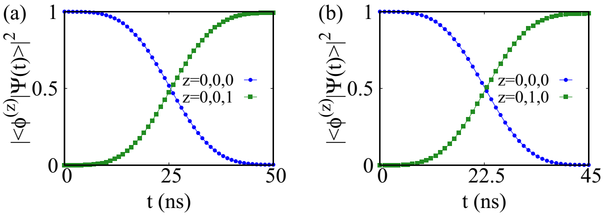

FIG. 15. Probabilities $p^{(z)}(t)$ for (a) $z = (0, 0, 0)$ and $z = (0, 0, 1)$ and (b) $z = (0, 0, 0)$ and $z = (0, 1, 0)$ as a function of time t. In both cases we use three basis states $N_m = 3$ to model the dynamics of the system, a control pulse of the form of Eq. (33), and a rise and fall time $T_{r/f}$ set to half the duration time T_d. (a) We use the drive frequency $\omega^D = 5.092$ GHz and the pulse amplitude $\delta/2\pi = 0.085$. (b) We use the drive frequency $\omega^D = 6.183$ GHz and the pulse amplitude $\delta/2\pi = 0.045$. The initial state of the system is always $|\psi^{(0,0,0)}\rangle$. Note that we were not able to activate these transitions in the effective model of architecture I [see Hamiltonian in Eq. (31)].

2. Circuit Hamiltonian simulations of transitions that are suppressed in the effective model

We start our discussion with a single, isolated flux-tunable transmon. The system itself is defined by the parameters in Table I and we model the system with the circuit Hamiltonian in Eq. (2). Here we consider the flux-tunable transmon with label $i = 2$. Figure 14(a) shows the time evolution of the probabilities $p^{(z)}(t)$, for the two lowest eigenstates $z \in \{0, 1\}$. We use a control pulse of the form of Eq. (33) [see Fig. 2(a)], where we set ω^{D} equal to the qubit frequency ω. The rise and fall time $T_{r/f}$ is set to half of the pulse duration T_d. The x axis displays the duration time. The pulse amplitude in this case is set to $\delta/2\pi = 0.001$. The system is initially in the state $|\phi^{(0)}\rangle$ and we are able to implement a smooth transition between the states $|\phi^{(0)}\rangle$ and $|\phi^{(1)}\rangle$.

Figure 14(b) shows the results for a similar scenario. Here we increase the amplitude by one order of magnitude; i.e., we use $\delta/2\pi = 0.01$. The time evolution shows that the duration T_d has decreased roughly by a factor of 10. Note that the transitions between the states $|\phi^0\rangle$ and $|\phi^1\rangle$ cannot be modeled with the effective Hamiltonian in Eq. (25).

In both cases it is sufficient to use three basis states to model the dynamics of the system; i.e., increasing the number of basis states above three has no real impact on the probabilities we are interested in.

While it is possible to generate similar results (data not shown) for amplitudes in the range $\delta/2\pi \in [0.001, 0.01]$ we find that for amplitudes $\delta/2\pi \gg 0.01$ it is not possible to implement a smooth transition between both states. Application of the pulse does not conserve the probability in the subspace $\{|\phi^{(0)}\rangle, |\phi^{(1)}\rangle\}$.

Next we study a system which consists of three transmons. We add two fixed-frequency transmons to the flux-tunable transmon. This means the corresponding circuit Hamiltonian is of the form of Eq. (7). Table I shows the corresponding system parameters. These parameters are motivated by a series of experiments reported in Ref. [3]. Figures 15(a) and 15(b) show the system's response to a harmonic pulse of the form of Eq. (33) [see Fig. 2(a)].

In Fig. 15(a) we use the drive frequency $\omega^D = 6.183$ and the amplitude $\delta/2\pi = 0.045$. Here the figure shows the probabilities $p^{(z)}(t)$, for $z = (0, 0, 0)$ and $z = (0, 1, 0)$, as a function of time t. In this case the intention is to drive the $z = (0, 0, 0) \rightarrow z = (0, 1, 0)$ transition.

Figure 15(b) shows a similar case. Here we use the drive frequency $\omega^D = 5.092$ and the amplitude $\delta/2\pi = 0.085$. Since we intend to drive the $z = (0, 0, 0) \rightarrow z = (0, 0, 1)$ transition, we display the corresponding probabilities $p^{(z)}(t)$ as a function of time t.

In both cases the initial state is set to $|\phi^{(0,0,0)}\rangle$ and we find a duration time T_d of around 50 ns.

Figures 15(a) and 15(b) show that we are able to implement transitions between the state pairs $z = (0, 0, 0)$ and $z = (0, 1, 0)$ as well as $z = (0, 0, 0)$ and $z = (0, 0, 1)$. In addition, it is also possible (data not shown) to drive transitions of the form $z = (0, 0, 1) \rightarrow z = (0, 1, 1)$ and $z = (0, 1, 0) \rightarrow z = (0, 1, 1)$, simply by changing the initial state of the system and leaving all other parameters. Note that we were not able to activate these transitions in the effective model of architecture I [see Hamiltonian in Eq. (31)]. Here we do not consider the transmon $i = 2$ (see Table I) since it is considered to be a coupler and not an actual qubit. However, it is possible to drive the transition $z = (0, 0, 0) \rightarrow z = (1, 0, 0)$.

For both cases we find that it is sufficient to use three transmon basis states to model the dynamics of the system.

3. Circuit Hamiltonian simulations of the unsuppressed transitions in the effective two-qubit models

We investigate the transitions which are unsuppressed in the effective model. Here we differentiate between two cases. We first discuss transitions which are used to implement two-qubit gates by means of harmonic microwave pulses (see Refs. [3,6,7]). In this case we simulate the circuit Hamiltonian in Eq. (7), with the parameters listed in Table I. As a second case, we study transitions which are activated by unimodal pulses, i.e., gates which are implemented by means of adiabatic passage techniques (see Refs. [5,34]). In this case we simulate the circuit Hamiltonian in Eq. (8). The corresponding system parameters can be found in Table II.

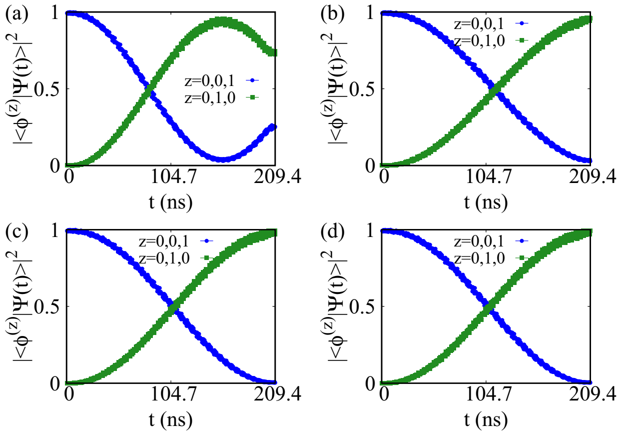

FIG. 16. Probabilities $p^{(0,0,1)}(t)$ and $p^{(0,1,0)}(t)$ as functions of time t. We use (a) $N_m = 3$, (b) $N_m = 4$, (c) $N_m = 6$, and (d) $N_m = 15$ basis states to model the system. We use a control pulse of the form of Eq. (33), with the pulse parameters $\omega^D = 1.089$ GHz, $T_{\mathrm{r/f}} = 13$ ns, and $\delta/2\pi = 0.075$. The pulse duration is $T_{\mathrm{d}} = 209.40$ ns. The system we simulate is defined by Eq. (7) and Table I. The $z = (0, 0, 1) \rightarrow z = (0, 1, 0)$ transition is often used to implement iSWAP operations (see Ref. [3]). We find that numerical accurate modeling of the dynamic behavior of the system seems to require at least $N_m = 6$ transmon basis states.

a. Architecture I

Figures 16(a)–16(d) show the time evolution of the probabilities $p^{(0,0,1)}(t)$ and $p^{(0,1,0)}(t)$ as a function of time t. We use $N_m = 3$ [Fig. 16(a)], $N_m = 4$ [Fig. 16(b)], $N_m = 6$ [Fig. 16(c)], and $N_m = 15$ [Fig. 16(d)] basis states to model the dynamics of the system. The transition we model here is often used to implement an iSWAP gate. The drive frequency is $\omega^{\mathrm{D}} = 1.089$ GHz, which corresponds roughly to the frequency difference $\Delta\omega = 1.100$ GHz between the individual transmon qubits $i = 1$ and $i = 0$. The frequency shift stems from the fact that the states $\{|\phi^{(z)}\rangle\}$ are not exact eigenstates of the full circuit Hamiltonian. The drive amplitude is set to $\delta/2\pi = 0.075$ and the initial state of the system is $|\phi^{(0,0,1)}\rangle$.

The time evolutions in Figs. 16(a)–16(d) clearly show that three or four basis states are not sufficient to describe this operation; i.e., if we compare the solutions in Figs. 16(a) and 16(b) with the reference solution in Figs. 16(c) or 16(d) we find substantial qualitative and quantitative differences. We find that we need at least six transmon basis states to model the system. Note that we simulated the same system as before when studying the single-qubit operations. We conclude that the number of states which is needed to model different types can vary; i.e., it is not a system property but it depends on the type of transition we simulate.

Figures 17(a)–17(d) show the time evolution of the probabilities $p^{(0,1,1)}(t)$ and $p^{(0,2,0)}(t)$ as a function of time t. We use $N_m = 3$ [Fig. 17(a)], $N_m = 4$ [Fig. 17(b)], $N_m = 8$ [Fig. 17(c)], and $N_m = 15$ [Fig. 17(d)] transmon basis states to model the system. This transition is often used to implement a CZ operation (see Ref. [13]). The corresponding drive frequency is $\omega^{\mathrm{D}} = 0.809$ GHz, which corresponds roughly to the energy difference, in gigahertz, of the two states involved. The pulse amplitude is $\delta/2\pi = 0.085$.

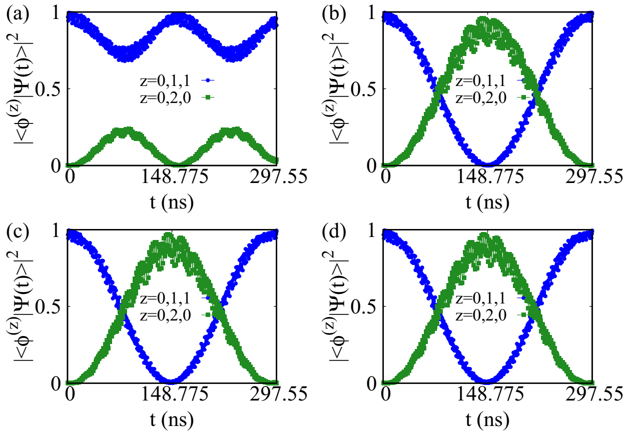

FIG. 17. Probabilities $p^{(0,1,1)}(t)$ and $p^{(0,2,0)}(t)$ as functions of time t. We use (a) $N_m = 3$, (b) $N_m = 4$, (c) $N_m = 8$, and (d) $N_m = 15$ basis states to model the system. We use a control pulse of the form of Eq. (33), with the pulse parameters $\omega^{\mathrm{D}} = 0.809$ GHz, $T_{\mathrm{r/f}} = 13$ ns, and $\delta/2\pi = 0.085$. The pulse duration is $T_{\mathrm{d}} = 297.55$ ns. The system we simulate is defined by Eq. (7) and Table I. The $z = (0, 1, 1) \rightarrow z = (0, 2, 0)$ transition is usually used to implement CZ operations (see Refs. [3,13]). We find that numerical accurate modeling of the dynamic behavior of the system seems to require at least $N_m = 8$ transmon basis states.

We observe that if we model this particular CZ operation, we find severe qualitative and quantitative deviations between the solutions in Figs. 17(a) and 17(b) and Figs. 17(c) or 17(d). Here we should use eight basis states to accurately model the dynamics of the system.

The iSWAP and CZ operations we studied here are implemented with gate durations T_{d} between 200 and 300 ns. It is possible to implement shorter gate durations, by increasing the amplitude (data not shown). However, this almost always means we have to increase the number of basis states, N_m, to obtain an accurate solution.

Furthermore, we repeated the same analysis for two additional devices. The corresponding device parameters were motivated by experiments carried out by the authors of Refs. [7,13,22]. Here we found similar results (data not shown), namely, that we need at least six or eight basis states to describe iSWAP and CZ operations, with similar gate durations.

The results we obtained for the iSWAP and CZ gates indicate that the influence of the higher levels $\{|\phi^{m>2}\rangle\}$ on the subspace $\{|\phi^{m\leqslant 2}\rangle\}$ is not negligible when it comes to modeling these operations. It seems to be the case that higher levels are instrumental in providing enough interaction strength, between the different subsystems, so that we can actually implement the operations [see Figs. 16(a) and 16(b) and Figs. 17(a) and 17(b) in particular]. Additionally, we can observe the trend that larger amplitudes seem to require more basis states N_m. Of course, all previous statements have to be restricted to the specific circuit Hamiltonian we studied here.

b. Architecture II

The second system we consider is defined by means of the circuit Hamiltonian in Eq. (8) and the parameters listed in

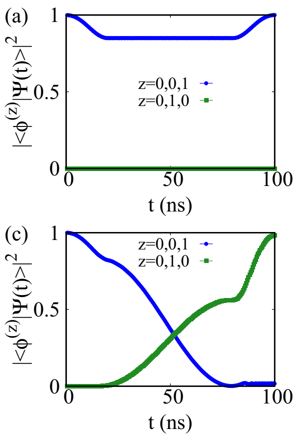

FIG. 18. Probabilities $p^{(0,0,1)}(t)$ and $p^{(0,1,0)}(t)$ as functions of time t. We use (a) $N_m = 3$, (b) $N_m = 4$, (c) $N_m = 14$, and (d) $N_m = 25$ basis states to model the system. We use a control pulse of the form of Eq. (33), with the pulse parameters $\omega^D = 0\,\text{GHz}$, $T_{\text{r/f}} = 20\,\text{ns}$, and $\delta/2\pi = 0.289$. The pulse duration is $T_{\text{d}} = 100.00\,\text{ns}$. The pulse is supposed to perform an iSWAP gate. The system we simulate is defined by Eq. (8) and Table II. The $z = (0, 0, 1) \rightarrow z = (0, 1, 0)$ transition might be used to implement iSWAP operations. Note that solutions in panels (a) and (b) do not have much in common with the reference solutions in panels (c) and (d).

Table II. Here we use a unimodal pulse (we set $\omega^D = 0$) of the form of Eq. (33) to implement two-qubit operations. Note that we apply the control pulse to the second flux-tunable transmon (see Table II, row $i = 1$).

Figures 18(a)–18(d) show the time evolution of $p^{(0,0,1)}(t)$ and $p^{(0,1,0)}(t)$ as functions of time t, for four different numbers of basis states $N_m = 3$ [Fig. 18(a)], $N_m = 4$ [Fig. 18(b)], $N_m = 14$ [Fig. 18(c)], and $N_m = 25$ [Fig. 18(d)}. We model a transition of the iSWAP type.

Obviously, Figs. 18(a) and 18(b) have not much in common with the reference solutions in Figs. 18(c) or 18(d). This means that if we use three or four states to model the system, we are not able to implement an iSWAP gate on this architecture. We need about 14 states to model this operation adequately. Additionally, note that during the time evolution $p^{(0,1,0)}(t) + p^{(0,0,1)}(t) \neq 1$ for various times t. The reason for this is that continuous population transfer takes place in the instantaneous basis.

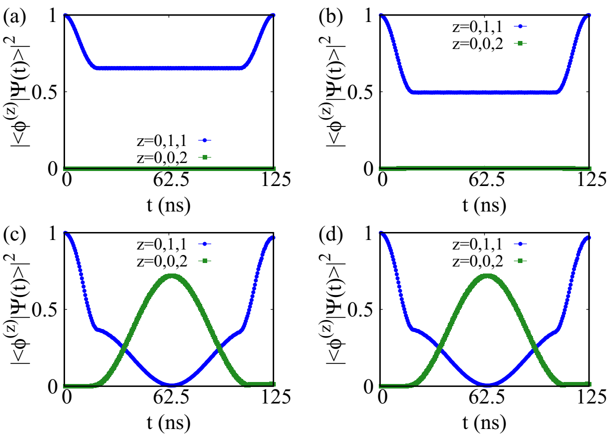

FIG. 19. Probabilities $p^{(0,1,1)}(t)$ and $p^{(0,0,2)}(t)$ as functions of time t. We use (a) $N_m = 3$, (b) $N_m = 4$, (c) $N_m = 16$, and (d) $N_m = 25$ basis states to model the system. We use a control pulse of the form of Eq. (33), with the pulse parameters $\omega^{\text{D}} = 0\,\text{GHz}$, $T_{\text{r/f}} = 20\,\text{ns}$, and $\delta/2\pi = 0.3335$. The pulse duration is $T_{\text{d}} = 125.00\,\text{ns}$. The pulse is supposed to perform a CZ gate. The system we simulate is defined by Eq. (8) and Table II. The $z = (0, 1, 1) \rightarrow z = (0, 0, 2)$ transition can be used to implement CZ operations (see Ref. [4]). Note that solutions in panels (a) and (b) do not have much in common with the reference solutions in panels (c) and (d).

The last case we study is the CZ gate, implemented on architecture II. Figures 19(a)–19(d) show the time evolution of the probabilities $p^{(0,1,1)}(t)$ and $p^{(0,0,2)}(t)$ as functions of time t, for $N_m = 3$ [Fig. 19(a)], $N_m = 4$ [Fig. 19(b)], $N_m = 16$ [Fig. 19(c)], and $N_m = 25$ [Fig. 19(d)].

In this case we implemented a slightly imperfect CZ operation; i.e., we implemented a pulse which ensures that $p^{(0,1,1)}(T_{\text{d}}) < 1$. A perfect CZ gate would only change the relative phase of the state vector but not the population. Therefore, modeling the system with three basis states would yield the same result as modeling the system with 25 states [see Fig. 19(a)]; i.e., it does not matter whether or not population exchange actually occurs. However, we want to determine the number of basis states which are needed to model the transitions $z = (0, 1, 1) \rightarrow (0, 0, 2)$ and $z = (0, 0, 2) \rightarrow (0, 1, 1)$. The easiest way to do this is to implement a slightly imperfect transition.

---

[1] C. A. Balanis, *Advanced Engineering Electromagnetics* (Wiley, New York, 2012)

[2] M. H. Devoret, in *Fluctuations quantiques*, edited by S. Reynaud, E. Giacobino, and J. Zinn-Justin, Les Houches Summer School, LXIII (Elsevier, Amsterdam, 1997), pp. 351–386.

[3] M. Ganzhorn, G. Salis, D. J. Egger, A. Fuhrer, M. Mergenthaler, C. Müller, P. Müller, S. Paredes, M. Pechal, M. Werninghaus, and S. Filipp, Phys. Rev. Research **2**, 033447 (2020).

[4] N. Lacroix, C. Hellings, C. K. Andersen, A. Di Paolo, A. Remm, S. Lazar, S. Krinner, G. J. Norris, M. Gabureac, J. Heinsoo, A. Blais, C. Eichler, and A. Wallraff, PRX Quantum **1**, 020304 (2020).

[5] L. DiCarlo, J. M. Chow, J. M. Gambetta, L. S. Bishop, B. R. Johnson, D. I. Schuster, J. Majer, A. Blais, L. Frunzio, S. M. Girvin, and R. J. Schoelkopf, Nature (London) **460**, 240 (2009).

[6] D. C. McKay, S. Filipp, A. Mezzacapo, E. Magesan, J. M. Chow, and J. M. Gambetta, Phys. Rev. Applied **6**, 064007 (2016).

[7] M. Roth, M. Ganzhorn, N. Moll, S. Filipp, G. Salis, and S. Schmidt, Phys. Rev. A **96**, 062323 (2017).

[8] X. Gu, J. Fernández-Pendás, P. Vikstål, T. Abad, C. Warren, A. Bengtsson, G. Tancredi, V. Shumeiko, J. Bylander, G. Johansson, and A. F. Kockum, PRX Quantum **2**, 040348 (2021).

[9] J. Koch, T. M. Yu, J. Gambetta, A. A. Houck, D. I. Schuster,

J. Majer, A. Blais, M. H. Devoret, S. M. Girvin, and R. J. Schoelkopf, Phys. Rev. A **76**, 042319 (2007).

[10] D. Willsch, M. Nocon, F. Jin, H. De Raedt, and K. Michielsen, Phys. Rev. A **96**, 062302 (2017).

[11] X. You, J. A. Sauls, and J. Koch, Phys. Rev. B **99**, 174512 (2019).

[12] R.-P. Riwar and D. P. DiVincenzo, npj Quantum Inf. **8**, 36 (2022).

[13] A. Bengtsson, P. Vikstål, C. Warren, M. Svensson, X. Gu, A. F. Kockum, P. Krantz, C. Križan, D. Shiri, I.-M. Svensson, G. Tancredi, G. Johansson, P. Delsing, G. Ferrini, and J. Bylander, Phys. Rev. Applied **14**, 034010 (2020).

[14] M. A. Rol, F. Battistel, F. K. Malinowski, C. C. Bultink, B. M. Tarasinski, R. Vollmer, N. Haider, N. Muthusubramanian, A. Bruno, B. M. Terhal, and L. DiCarlo, Phys. Rev. Lett. **123**, 120502 (2019).

[15] A. Blais, A. L. Grimsmo, S. M. Girvin, and A. Wallraff, Rev. Mod. Phys. **93**, 025005 (2021).

[16] S. Krinner, S. Lazar, A. Remm, C. K. Andersen, N. Lacroix, G. J. Norris, C. Hellings, M. Gabureac, C. Eichler, and A. Wallraff, Phys. Rev. Applied **14**, 024042 (2020).

[17] *Quantum Information Processing*, edited by D. DiVincenzo, Schriften des Forschungszentrums Jülich. Reihe Schlüsseltechnologien/Key Technologies, Vol. 52 (Forschungszentrum Jülich GmbH Zentralbibliothek Verlag, Jülich, 2013).

[18] F. Yan, P. Krantz, Y. Sung, M. Kjaergaard, D. L. Campbell, T. P. Orlando, S. Gustavsson, and W. D. Oliver, Phys. Rev. Applied **10**, 054062 (2018).

[19] A. J. Baker, G. B. P. Huber, N. J. Glaser, F. Roy, I. Tsitsilin, S. Filipp, and M. J. Hartmann, Appl. Phys. Lett. **120**, 054002 (2022).

[20] S. Weinberg, *Lectures on Quantum Mechanics*, 2nd ed. (Cambridge University Press, Cambridge, U.K., 2015).

[21] M. H. S. Amin, Phys. Rev. Lett. **102**, 220401 (2009).

[22] M. Roth, Ph.D. thesis, RWTH Aachen University, 2019.

[23] D. Willsch, Ph.D. thesis, RWTH Aachen University, 2020.

[24] H. Lagemann, JUelich Superconducting QUAntum Computer Emulator - JUSQUACE, software available from https://jugit.fz-juelich.de/qip/jusquace.

[25] www.gauss-centre.eu.

[26] Jülich Supercomputing Centre, J. Large-Scale Res. Facil. **5**, A135 (2019).

[27] M. Willsch, Ph.D. thesis, RWTH Aachen University, 2020.

[28] D. Burgarth, P. Facchi, G. Gramegna, and K. Yuasa, Quantum **6**, 737 (2022).

[29] N. Didier, E. A. Sete, M. P. da Silva, and C. Rigetti, Phys. Rev. A **97**, 022330 (2018).

[30] B. Foxen, C. Neill, A. Dunsworth, P. Roushan, B. Chiaro, A. Megrant, J. Kelly, Z. Chen, K. Satzinger, R. Barends, F. Arute, K. Arya, R. Babbush, D. Bacon, J. C. Bardin, S. Boixo, D. Buell, B. Burkett, Y. Chen, R. Collins, and J. M. Martinis (Google AI Quantum), Phys. Rev. Lett. **125**, 120504 (2020).

[31] M. Suzuki, Proc. Jpn. Acad., Ser. B **69**, 161 (1993).

[32] H. De Raedt, Comput. Phys. Rep. **7**, 1 (1987).

[33] J. Huyghebaert and H. De Raedt, J. Phys. A: Math. Gen. **23**, 5777 (1990).

[34] N. V. Vitanov, T. Halfmann, B. W. Shore, and K. Bergmann, Annu. Rev. Phys. Chem. **52**, 763 (2001).